CHALMERS
UNIVERSITY OF TECHNOLOGY

Three-Dimensional Finite-Difference Time-Domain Modeling of Road Traffic Noise

Master's thesis in Sound and Vibration

MAX GREN
STAFFAN HEIKER

DEPARTMENT OF ARCHITECTURE AND CIVIL ENGINEERING
CHALMERS UNIVERSITY OF TECHNOLOGY
Gothenburg, Sweden 2021
www.chalmers.se

Master's thesis 2021

Three-Dimensional Finite-Difference Time-Domain Modeling of Road Traffic Noise

MAX GREN
STAFFAN HEIKER

CHALMERS
UNIVERSITY OF TECHNOLOGY

Department of Architecture and Civil Engineering
Division of Applied Acoustics
Chalmers University of Technology
Gothenburg, Sweden 2021

Three-Dimensional Finite-Difference Time-Domain Modeling of Road Traffic Noise
MAX GREN and STAFFAN HEIKER

Supervisor: Jens Forssén, Department of Civil and Environmental Engineering
Examiner: Astrid Pieringer, Department of Civil and Environmental Engineering

Master's Thesis 2021
Department of Architecture and Civil Engineering
Division of Applied Acoustics
Chalmers University of Technology
SE-412 96 Gothenburg
Telephone +46 31 772 1000

Cover: Simulated wave propagation, calculated using FDTD.

Typeset in LaTeX
Printed by Chalmers Reproservice
Gothenburg, Sweden 2021

Three-Dimensional Finite-Difference Time-Domain Modeling of Road Traffic Noise
MAX GREN and STAFFAN HEIKER
Department of Civil and Environmental Engineering
Chalmers University of Technology

Abstract

With today's rapid expansion and densification of urban areas, the amount of people living in close proximity to loud infrastructure on a daily basis is steadily increasing, which prompts a greater demand for control and prevention of traffic noise. Sufficiently detailed models of sound propagation in urban areas that are applicable to residential buildings are therefore in high demand and calls for further development.

The aim of this study is therefore to design a three-dimensional Finite-Difference Time-Domain model for calculating and visualizing sound propagation in an outdoor environment, with the ability to implement both rigid and finite-mass objects for construction of building elements. Modeling of indoor sound pressure caused by an outdoor sound source is also a desired outcome. By establishing a model in Matlab, mainly consisting of sound pressure and velocity variables arranged in staggered grids, a foundation for performing a series of tests using noise screen and absorptive room models was established. The models were subsequently validated using analytical solutions for cases corresponding to the tests simulated in the model environment.

The results from this study show that the rigid objects implemented in the model functioned properly with regards to the validating theoretical models, as well as the finite-mass wall and screen according to the mass law. Also, it was found that using artificial thick absorbing layers as sound absorbers functioned sufficiently well for simulating an acoustic environment appropriate for a residential room.

Using the knowledge gained from this continuation of previous studies on the subject can serve as a useful tool for estimating traffic noise levels indoors, as well as a foundation for further development of the model and future studies of three-dimensional FDTD modeling of outdoor sound propagation.

Keywords: traffic noise, three-dimensional, Finite-Difference Time-Domain, sound propagation, discretization, absorption, finite-mass

Acknowledgements

First and foremost, we would like to extend our gratitude to our supervisor Jens Forssén, who provided us with valuable assistance and guidance throughout the project.
We would also like to thank our opponent and colleague Gustav Vågfelt for his feedback and constructive comments during the presentation of this project.
Finally, we would like to acknowledge all of our other friends, colleagues and teachers at Applied Acoustics, who always offer their help, support and good company.

Max Gren and Staffan Heiker, Gothenburg, July 2021

Contents

List of Figures

1

Introduction

Predicting sound propagation in various environments can be difficult due to the vastness and unpredictability of the usual outdoor conditions that occur in the field of urban acoustics and community noise. It is, however, of great importance to be able to correctly, efficiently and carefully represent the actual surroundings that affect the propagation and spreading of sound in outdoor and urban environments.

Finite-Difference Time-Domain (FDTD) methods are used for solving fluid dynamic problems formulated as differential equations, through spatial and temporal discretization. Since a large number of real-life parameters can be taken into consideration with FDTD, it is a powerful approach for modeling outdoor sound propagation in complex environments. However, the drawbacks of this method consist of long computation times and difficulties to implement time domain boundary conditions [1]. These properties also prompt the less frequent use of three dimensional models and visualization, although such studies have been performed by Symons et al. [2] for example.

There are also various methods for describing, predicting and evaluating outdoor sound propagation other than FDTD, such as the *Parabolic Equation* (PE), the *Fast Field Program* (FFP) as well as combined methods like the FDTD-PE solution proposed by Van Renterghem and Botteldooren [3]. The latter is described by the authors as less computationally intensive than FDTD when considering a propagation area with several complex reflecting objects in the near vicinity of the source. The FFP method was originally developed for predicting wave propagation in the sea but later readjusted for propagation in air [4] and is, like the Parabolic Equation, based in the frequency domain.

1.1 Background

Along with the industrialization during the last centuries, the exposure to noise has increased dramatically in the everyday life of the population. It has become such a natural part of human life that many people may not reflect upon the discomfort it causes and the consequences it could have. Generally, the discomfort grows with increased noise levels and prolonged exposure and it can develop into disease and ultimately early death. Due to the negative health and environmental effects of noise, the European Commission as well as national authorities around Europe have decided on regulations in several acoustic areas to limit the community noise levels.

One of the most prominent noise sources in modern society is road traffic and it is advantageous to be able to predict the traffic noise levels. Since today's urban areas experience a constant and intensive expansion and densification, more people are subjected to high levels of traffic noise on a daily basis. This is a strong and clear incitement for improvements in controlling, preventing and regulating major traffic noise sources. Finding solutions to high noise levels as early as in the planning stage of a project can reduce costs significantly compared to taking action at later stages. Consequently, several prediction methods have been developed and further development could be of great value in the field of urban planning.

1.2 Aim

The aim of this study is to provide an accurate tool for estimating and predicting the effect of road traffic noise in a simulated three-dimensional urban environment with high complexity. To do so, a 3D FDTD model of an outdoor area is implemented in Matlab, where objects with a finite mass can be modeled to represent walls, facades and noise screens. Additionally, thick absorbing boundaries, which also constitute the boundaries of the model, are introduced as sound absorbers that serve to enable calculating the reverberation time in a room constructed in the model.

2

Theory

In the following sections, FDTD methods and their relation to auralization of sound in a moving medium are described, which also establishes their function in models of real-life conditions. Conditions and elements that affect sound propagation in outdoor environments, such as wind and temperature gradients, turbulence and obstacles that are implemented with intent to affect the path of the sound propagation are discussed to the extent of which they apply to said models. Objects that occur in urban environments and their role in affecting sound propagation paths, such as noise barriers and buildings, are described. The essential characteristics of FDTD methods in a three-dimensional space are presented, such as the extension of spatial discretization for a third spatial dimension and advancing the Finite-Difference solution forward in time through temporal discretization. Additionally, the derivation and implementation of absorbing boundary conditions for realistic modeling of the limits in the forthcoming model environments are presented.

2.1 Discretization

Both spatial and temporal discretization of FDTD grids are well documented subjects when considering two spatial dimensions. Most of the information used in this study on the subject is based on theory gathered by Ostashev [1], who comprehensively covered a large part of the mathematics behind the foundation of this method. Other sources for detailed descriptions of spatial and temporal discretization using two spatial dimensions include Wilson and Liu [5], who delivered a more explicit derivation of various methods for temporal discretization in particular.

FDTD methods work on the principle of discretizing temporal and spatial derivatives using grids, whose nodes are locations for storing the values of those derivatives. The grids are placed offset, or staggered, relative to each other, in both space and time. In an acoustic context, the grid nodes are used to store acoustic pressure variables and source properties, as well as acoustic particle velocities and wind gradient components. When using a sound source, the location for storing and evaluation of the source is determined by the type of source. A mass source would generally be evaluated in the pressure grid, while the components of a force source is typically evaluated along with the corresponding velocity components [1]. Combining spatial and temporal discretization ultimately allows advancement of the grid structures in time, which can be analyzed in the time domain.

2.1.1 Spatial Discretization in 3D

Ostashev's and Wilson's [1][6] derivations of the acoustic pressure and particle velocity temporal derivatives originate from a set of linearized equations of fluid dynamics, rearranged into two coupled difference equations for a pressure variable p and an acoustic particle velocity variable $\mathbf{w}$. Several authors apply those expressions in a two-dimensional plane to act as a common starting point for 2D FDTD calculations of sound propagation [1][5][6]. The temporal derivatives can be written as

$$\frac{\partial p}{\partial t} = -(\mathbf{v} \cdot \nabla)p - K\nabla \cdot \mathbf{w} + KQ \tag{2.1}$$

and

$$\frac{\partial \mathbf{w}}{\partial t} = -(\mathbf{v} \cdot \nabla)\mathbf{w} - (\mathbf{w} \cdot \nabla)\mathbf{v} - b\nabla p + b\mathbf{F} \tag{2.2}$$

with $\mathbf{v}$ as the medium velocity in air, b as the mass buoyancy of air, i.e. the inverse of the air density, K as the adiabatic bulk modulus, where $K = \rho c^2$, Q as a mass source and $\mathbf{F}$ as a force source. In Equations (2.1) and (2.2), $\mathbf{v}$, $\mathbf{w}$ and $\mathbf{F}$ are described as two-dimensional vectors consisting of x and y components. The vectors can be applied in three-dimensional space by extending them by a third spatial component z. This entails implementation of additional particle and medium velocity components in the z dimension, along with mixed derivative terms as a result of multiplication between their vectors and gradient vectors.

Ostashev and Wilson [1] describe a series of methods for discretizing the pressure and velocity quantities both spatially and temporally using a staggered grid structure, which are also discussed by Wilson and Liu [5]. Temporal discretization using unstaggered grids is also mentioned by Ostashev and Wilson as the most straightforward method of temporal discretization, but deemed less preferable due to its instability and increased memory requirements. The spatial discretization part of FDTD methods serve to create a basis for calculating differences between the spatial derivatives in the nodes of the pressure and velocity grids. In the case presented by Ostashev and Wilson [1], the positions of the nodes that store the acoustic pressure p in the pressure grid are assigned to and indicated by integers. Each node position is thereby given by integers i and j, along with the grid spaces Δx and Δy, as $(x, y) = (i\Delta x, j\Delta y)$. The corresponding nodes of the grid storing the particle velocities w are offset by half a grid step in each spatial dimension.

Figure 2.1 shows the two-dimensional pressure and velocity grids, where the latter is offset from the pressure grid by half of an integer step in both the x and y dimensions.

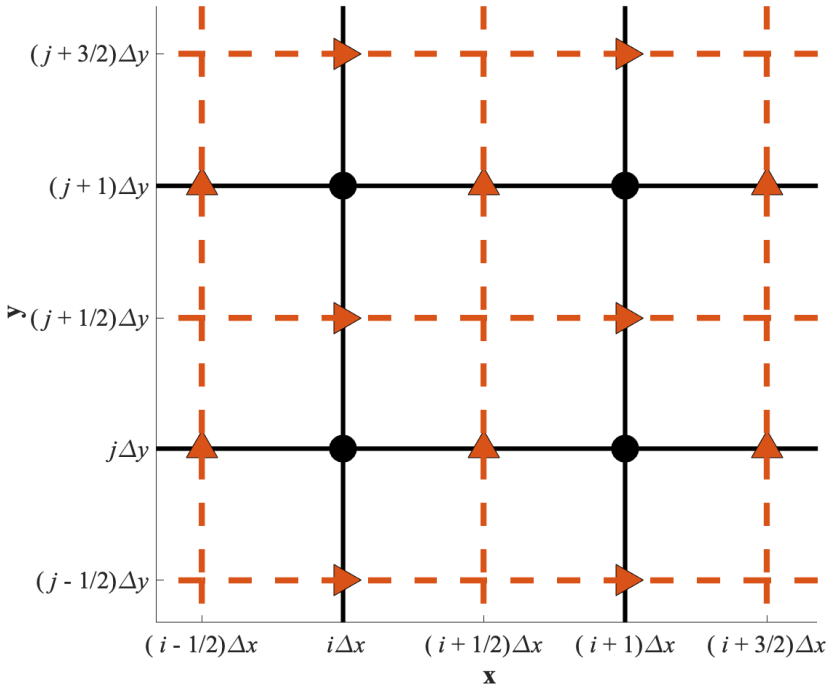

Figure 2.1: Spatially staggered pressure and velocity grids. The pressure grid consists of solid lines and the dashed lines belong to the velocity grid.

The derivatives of the acoustic pressure, along with the components of the particle velocity and wind gradients, are used to calculate centered differences across each grid step. Figure 2.1 uses arrows to illustrate how the velocity derivatives are aligned with integer values in each dimension. By extending Ostashev's and Wilson's [1] expansions of Equations (2.1) and (2.2) into three spatial dimensions, the expressions consisting of the various derivatives,

$$\frac{\partial p}{\partial t} = -v_x\frac{\partial p}{\partial x} - v_y\frac{\partial p}{\partial y} - v_z\frac{\partial p}{\partial z} - K\frac{\partial w_x}{\partial x} - K\frac{\partial w_y}{\partial y} - K\frac{\partial w_z}{\partial z} - KQ, \tag{2.3}$$

$$\frac{\partial w_x}{\partial t} = -v_x\frac{\partial w_x}{\partial x} - v_y\frac{\partial w_x}{\partial y} - v_z\frac{\partial w_x}{\partial z} - w_x\frac{\partial v_x}{\partial x} - w_y\frac{\partial v_x}{\partial y} - w_z\frac{\partial v_x}{\partial z} - b\frac{\partial p}{\partial x}, \tag{2.4}$$

$$\frac{\partial w_y}{\partial t} = -v_x\frac{\partial w_y}{\partial x} - v_y\frac{\partial w_y}{\partial y} - v_z\frac{\partial w_y}{\partial z} - w_x\frac{\partial v_y}{\partial x} - w_y\frac{\partial v_y}{\partial y} - w_z\frac{\partial v_y}{\partial z} - b\frac{\partial p}{\partial y} \tag{2.5}$$

and

$$\frac{\partial w_z}{\partial t} = -v_x\frac{\partial w_z}{\partial x} - v_y\frac{\partial w_z}{\partial y} - v_z\frac{\partial w_z}{\partial z} - w_x\frac{\partial v_z}{\partial x} - w_y\frac{\partial v_z}{\partial y} - w_z\frac{\partial v_z}{\partial z} - b\frac{\partial p}{\partial z}, \tag{2.6}$$

are obtained. For the partial derivatives of w in Equations (2.4) – (2.6), the terms including the aforementioned force source $\mathbf{F}$ are omitted and only the point source Q is taken into account in this study. These equations are also applicable for non-moving media, in which each term containing any components of the gradient of the medium velocity in air, $\mathbf{v}$, is omitted.

Figure 2.2 illustrates the principal extension of Figure 2.1 into three spatial dimensions via the expressions in Equations (2.3) – (2.6). The spatial staggering of the velocity grid in the z dimension is analogous to the corresponding shift in the x and y dimensions represented in Figure 2.1.

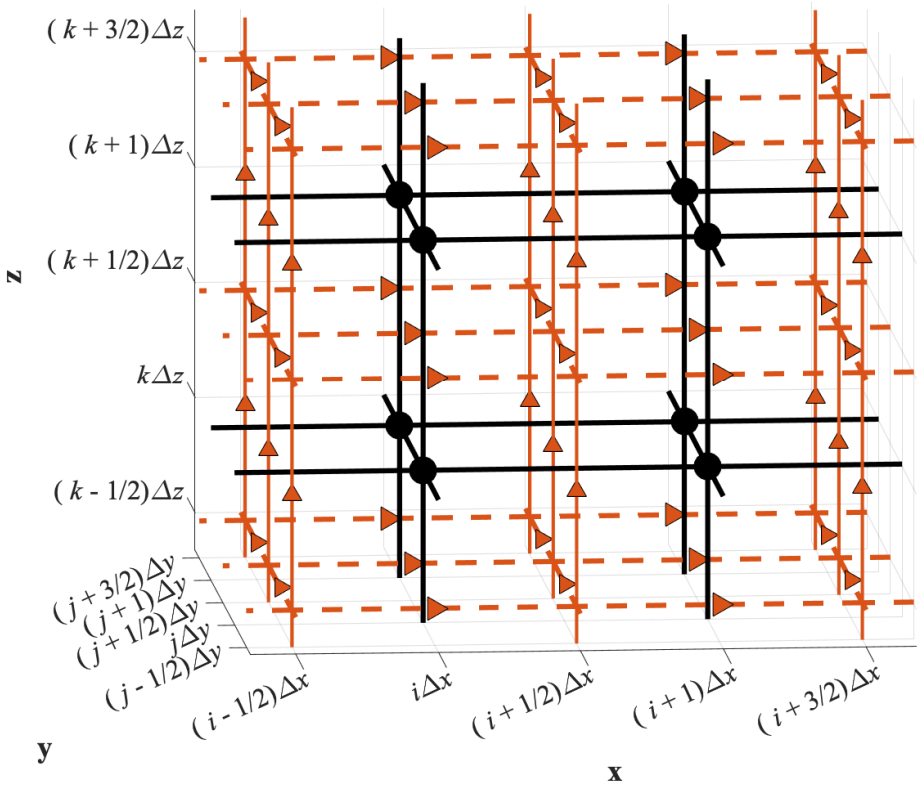

Figure 2.2: Spatially staggered grid in three-dimensional space. The pressure grid consists of solid, black lines. The dashed grids connected by solid lines store the velocity quantities $\mathbf{v}$ and $\mathbf{w}$.

As seen in the figure, the relations between the grids in the z dimension are equal to those presented in the x and y dimensions and staggered by a half-integer step in the z dimension as well. The arrows plotted on the vertical axes of the velocity grid also indicate that the z components of the velocity terms are averaged to be evaluated in the integer positions.

Formulas [12.6] – [12.12] in [1] present examples on how to estimate some of the terms given in Equations (2.3) – (2.6). Essentially, each term is calculated between the two nodes in which its values are stored by averaging by their intermediate distance in the grid. By themselves, the partial derivatives are simply evaluated as, for example,

$$\frac{\partial p}{\partial x}((i+1/2)\Delta x, j\Delta y, k\Delta z, t) \simeq \frac{p((i+1)\Delta x, j\Delta y, k\Delta z, t) - p(i\Delta x, j\Delta y, k\Delta z, t)}{\Delta x}, \tag{2.7}$$

$$\frac{\partial w_x}{\partial x}(i\Delta x, j\Delta y, k\Delta z, t) \simeq \frac{w_z((i+1/2)\Delta x, j\Delta y, k\Delta z, t) - w_z((i-1/2)\Delta x, j\Delta y, k\Delta z, t)}{\Delta x} \tag{2.8}$$

or

$$\frac{\partial w_z}{\partial z}(i\Delta x, j\Delta y, k\Delta z, t) \simeq \frac{w_z(i\Delta x, j\Delta y, (k+1/2)\Delta z, t) - w_z(i\Delta x, j\Delta y, (k-1/2)\Delta z, t)}{\Delta z}, \tag{2.9}$$

where the partial derivative of the pressure, $\partial p/\partial x$, is evaluated at a half-integer position in the grid as an average of two adjacent integer position values. The particle velocity components, $\partial w_x/\partial x$ and $\partial w_z/\partial z$, are averaged between half-integer node values in their respective dimensions and evaluated in integer node positions. The combined terms that appear in Equations (2.3) – (2.6) containing components of the wind speed gradient, $\mathbf{v}$, are estimated in several steps that vary based on where each quantity is stored. To estimate a centered difference around, for instance, $v_x(\partial p/\partial x)$ at $(x, y, z) = (i\Delta x, j\Delta y, k\Delta z, t)$, Ostashev and Wilson [1] evaluate v_x and $\partial p/\partial x$ in the same node positions as

$$\begin{aligned} v_x\left(\frac{\partial p}{\partial x}\right)(i\Delta x, j\Delta y, k\Delta z, t) \simeq & \\ & \frac{1}{2\Delta x}(v_x((i+1/2)\Delta x, j\Delta y, k\Delta z, t) \\ & \cdot (p((i+1)\Delta x, j\Delta y, k\Delta z, t) - p(i\Delta x, j\Delta y, k\Delta z, t)) \\ & + v_x((i-1/2)\Delta x, j\Delta y, k\Delta z, t) \\ & \cdot (p(i\Delta x, j\Delta y, k\Delta z, t) - p((i-1)\Delta x, j\Delta y, k\Delta z, t))) \end{aligned} \tag{2.10}$$

where $\partial p/\partial x$ is averaged at $(x, y, z) = ((i+1/2)\Delta x, j\Delta y, k\Delta z, t)$ and $(x, y, z) = ((i-1/2)\Delta x, j\Delta y, k\Delta z, t)$ in order to be evaluated in the same nodes as v_x. Similarly,

the mixed term $v_x\,(\partial w_x/\partial x)$, which is estimated at $(x, y, z) = ((i + 1/2)\Delta x, j\Delta y, k\Delta z, t)$, averages the separate terms v_x and $(\partial w_x/\partial x)$ across both $(x, y, z) = ((i + 1)\Delta x, j\Delta y, k\Delta z, t)$ and $(x, y, z) = (i\Delta x, j\Delta y, k\Delta z, t)$. Those averages are then used to estimate $v_x\,(\partial w_x/\partial x)$ at the aforementioned half-integer node position. The same procedure is also applied when evaluating $v_y\,(\partial w_y/\partial y)$ and $v_z\,(\partial w_z/\partial z)$ by averaging across grid steps in the corresponding dimensions.

2.1.2 Temporal Discretization in 3D

After establishing the spatially staggered pressure and velocity grids and discretizing in three dimensional space, the next part of the discretization process is to advance the variables of the wave field in time. Ostashev and Wilson [1][6], as well as Wilson and Liu [5], discuss methods of temporal discretization using both staggered and unstaggered velocity grids, where the velocity variables are stored either on the same time level as the pressure, or in nodes offset from the pressure grid by a half-integer time step.

Figure 2.3 illustrates the concept of temporally staggering the velocity grid. In principle, it works similarly to spatial staggering, which becomes apparent due to the likeness of Figure 2.3 to Figure 2.1.

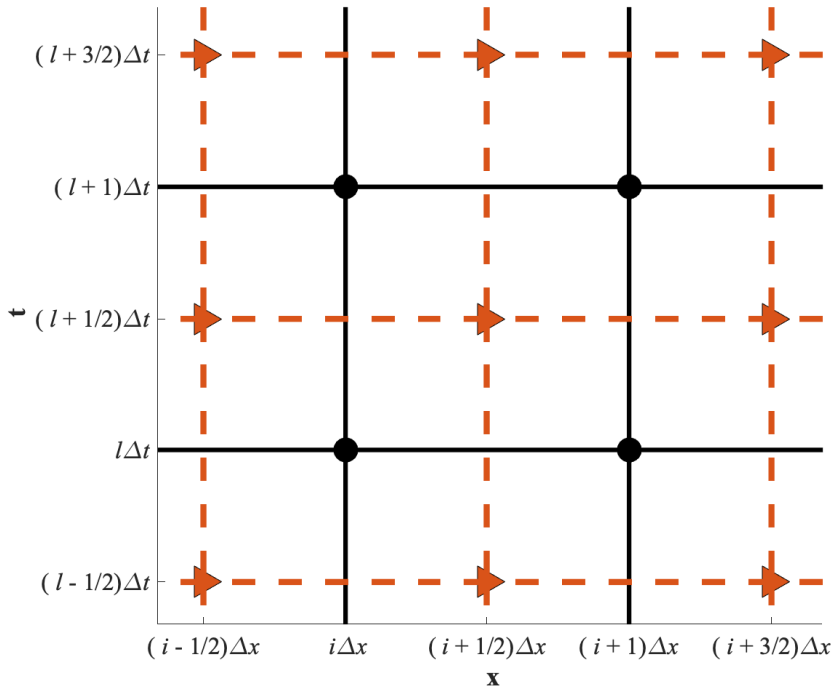

Figure 2.3: Temporally staggered pressure and velocity grids. The pressure grid consists of solid lines and the dashed lines belong to the velocity grid. For clarity and simplicity, only one spatial dimension is presented in this figure.

Ostashev and Wilson [1] abbreviate the right side of Equation (2.1) to f_p and the spatial components of (2.2) to f_x, f_y and f_z. The pressure variables, stored at the integer nodes, are as in the case of spatial discretization estimated by averaging over time steps, as

$$\begin{aligned} p(i\Delta x, j\Delta y, k\Delta z, (l+1)\Delta t) \simeq p(i\Delta x, j\Delta y, k\Delta z, l\Delta t) \\ + \Delta t f_p(i\Delta x, j\Delta y, k\Delta z, (l+1/2)\Delta t), \end{aligned} \tag{2.11}$$

where p is centered in time at $t = l\Delta t$. For the particle velocity components, t is centered at $t = (l + 1/2)\Delta t$ and is estimated as

$$\begin{aligned} w_x((i+1/2)\Delta x, j\Delta y, k\Delta z, (l+1/2)\Delta t) \simeq \\ w_x((i+1/2)\Delta x, j\Delta y, k\Delta z, (l-1/2)\Delta t) \\ + \Delta t f_x((i+1/2)\Delta x, j\Delta y, k\Delta z, l\Delta t), \end{aligned} \tag{2.12}$$

which is done in a corresponding fashion when estimating the w_y and w_z components, as

$$\begin{aligned} w_y(i\Delta x, (j+1/2)\Delta y, k\Delta z, (l+1/2)\Delta t) \simeq \\ w_y(i\Delta x, (j+1/2)\Delta y, k\Delta z, (l-1/2)\Delta t) \\ + \Delta t f_y(i\Delta x, (j+1/2)\Delta y, k\Delta z, l\Delta t) \end{aligned} \tag{2.13}$$

and

$$\begin{aligned} w_z(i\Delta x, j\Delta y, (k+1/2)\Delta z, (l+1/2)\Delta t) \simeq \\ w_z(i\Delta x, j\Delta y, (k+1/2)\Delta z, (l-1/2)\Delta t) \\ + \Delta t f_z(i\Delta x, j\Delta y, (k+1/2)\Delta z, l\Delta t). \end{aligned} \tag{2.14}$$

These expressions are, when considering a moving medium, abbreviated by Ostashev in Equations [12.23] and [12.24], [1] into

$$\mathbf{P}_{l+1} = \mathbf{P}_l + \Delta t \dot{\mathbf{P}}_{l+1/2}(\mathbf{P}_{l+1/2}\mathbf{W}_{l+1/2}) \tag{2.15}$$

and

$$\mathbf{W}_{l+1/2} = \mathbf{W}_{l-1/2} + \Delta t \dot{\mathbf{W}}_l(\mathbf{W}_l\mathbf{P}_l), \tag{2.16}$$

where $\mathbf{P}_l$ and $\mathbf{W}_l$ are described as vectors that contain acoustic pressures and velocities, respectively, in all grid node positions at $t = l\Delta t$. The terms $\dot{\mathbf{P}}$ and $\dot{\mathbf{W}}$ represent their time derivatives. The mixed terms containing components of the medium velocity v are also incorporated into those terms. This is often referred to as the *staggered leapfrog* method, by Ostashev among others, because of how the variables stored in the half-integer nodes advance in an alternating pattern contrary to the variables in the integer nodes [1][5][6].

2.1.3 The Courant Condition

In order to produce accurate results, the model requires a convergence condition that governs the discretization in space and time. The Courant number is one such condition and is given by a relation between the temporal and spatial grid spacing as

$$C = \frac{u\Delta t}{\Delta r}, \tag{2.17}$$

where u is the speed of the sound propagation in air and, for a non-uniform grid, $\Delta r = 1/\sqrt{(\Delta x)^{-2} + (\Delta y)^{-2} + (\Delta z)^{-2}}$ [1]. For numerical stability, FDTD models has to satisfy the Courant condition, $C << 1$, which may be an issue concerning the practicality of the calculations. The spatial step-size has to be much smaller than a wavelength for accurate calculations [1]. Consequently, if high frequencies are of interest, the time steps has to be very small in order to satisfy the Courant condition, resulting in increased computational times.

Van Renterghem [7] states that dispersion, i.e. non-spherical spreading of the waves, is an inherent error that follows with the implementation of FDTD and that the error is largest along the coordinate axes. For both accuracy and numerical efficiency, he suggests using a Courant number of exactly 1 and, as a rule of thumb, having at least 10 nodes per wavelength for the highest frequency of interest.

Since the wind gradient affects the speed of the wave propagation and thereby the wavelength, the grid spacing has to be adjusted for a moving medium to maintain accuracy at high frequencies. For propagation in a uniformly moving medium, i.e. v_x v_y and/or v_z are constants separated from zero, the speed $u = u_+ = c_0 + v$ in the downwind direction, while for the upwind direction $u = u_- = c_0 - v$ [1]. It follows from the relation $\lambda = u/f$ that the wavelength is shortest in the upwind direction and, as mentioned, the grid spacing is decided by the shortest wavelength of interest. Ostashev [1] uses the Mach number $M = v/c$ to describe a general relation between Δr and λ as

$$\Delta r = \frac{\lambda_-}{N} = \frac{\lambda}{N}(1 - M) \tag{2.18}$$

where N denotes the number of nodes in the grid per wavelength, with respect to the upwind direction of the sound field. The wind speed is largest in the downwind direction. Therefore, the downwind sets an upper limit to the temporal spacing, since

$$\Delta t < \frac{\lambda_-}{Nu_+} = \frac{1}{Nf}\frac{1 - M}{1 + M} \tag{2.19}$$

according to the Courant condition [1]. Although, for a motionless medium, M is

set to 0, which is the condition that constitutes the least constrictive requirement for the size of the time step Δt. In that sense, a motionless medium can be the most computationally efficient form of an FDTD model, but also one that requires refining for maximum adaptability.

2.2 Boundary Conditions

In any model based on a numerical method, it is of high importance to define the limits and boundaries of the conditions that apply within the perimeter of the model, in order to practically and efficiently delimit the range of the computations. One of the main motivations for implementing boundary conditions in the case of outdoor sound propagation, where the edges of the model do not represent the walls of a closed space, is to avoid any reflections caused by the edges [7][1]. Naturally, if not eliminated, the edges work as acoustically hard surfaces. The reflections affect the sound field in the model and significantly reduce its likeness to real-life outdoor conditions. To avoid unwanted reflections, artificial absorbing layers, usually referred to as *absorbing boundary conditions* (ABC) are often implemented at the boundaries of FDTD models [5].

2.2.1 Absorbing Boundary Conditions

There are several methods for implementing absorbing boundary conditions to FDTD models available in literature. In Equations (12.44) – (12.59), Ostashev [1] gives a detailed description of the theory and implementation of *perfectly matched layers* (PML) as boundary conditions for a two-dimensional space. The PML method was introduced by Berenger [8] and is based on a complex coordinate transform that results in the ability to implement particularly thin absorbing layers that require a small amount of space in the model. The formulation of the PML transform given by Ostashev [1] is, however, presented as quite computationally tedious even when applied in a non-moving medium in only two spatial dimensions.

A more straight-forward, however less space efficient, approach for implementing ABC is to add thick absorbing layers at the model boundaries. By modifying the flow resistivity in the nodes near the model edges, the energy is gradually reduced as the waves propagate through the artificial absorbers toward the edges, ultimately resulting in zero reflections. Wilson and Liu [5] describes a method to implement such layers in FDTD codes, starting with an expression for the reflection coefficient of a wave propagating in a fluid into a solid medium in Equation (2.20) and Snell's law in Equation (2.21),

$$R = \frac{Z_\mathrm{c} \cos\theta_\mathrm{i} - \rho c \cos\theta_\mathrm{t}}{Z_\mathrm{c} \cos\theta_\mathrm{i} + \rho c \cos\theta_t} \tag{2.20}$$

$$k \sin\theta_\mathrm{i} = k_c \sin\theta_\mathrm{t} \tag{2.21}$$

where Z_c is the complex impedance for wave propagation in the solid material, c is the speed of wave propagation in the fluid, k is the wave number in the fluid, k_c is the complex wave number in the solid, θ_i is the angle of incidence and θ_t is the angle of the transmitted wave relative to the surface normal [5]. From here on, the wave will be assumed to be sound, the fluid is air and the solid is an absorbing layer. If $R = 0$, i.e. no reflections occur at the layer, then

$$Z_\mathrm{c} \cos\theta_\mathrm{i} = \rho c \cos\theta_\mathrm{t}. \tag{2.22}$$

By combining the squares of Equations (2.21) and (2.22), the θ_t can be eliminated. Equation (2.21) implies that

$$\left(\frac{k}{k_\mathrm{c}}\right)^2 \sin^2\theta_\mathrm{i} - \sin^2\theta_\mathrm{t} = 0 \tag{2.23}$$

and from Equation (2.22) follows

$$\left(\frac{Z_\mathrm{c}}{\rho c}\right)^2 \cos^2\theta_\mathrm{i} - \cos^2\theta_\mathrm{t} = 0, \tag{2.24}$$

hence

$$\left(\frac{Z_\mathrm{c}}{\rho c}\right)^2 \cos^2\theta_\mathrm{i} + \left(\frac{k}{k_\mathrm{c}}\right)^2 \sin^2\theta_\mathrm{i} = \cos^2\theta_\mathrm{t} + \sin^2\theta_\mathrm{t} = 1. \tag{2.25}$$

The complex wavenumber and impedance of the can be written in terms of angular frequency, ω, complex density, ρ_c and adiabatic bulk, κ_e as

$$k_\mathrm{c} = \omega\sqrt{\frac{\rho_\mathrm{c}}{\kappa_\mathrm{e}}} \tag{2.26}$$

and

$$Z_c = \sqrt{\kappa_\mathrm{e}\rho_\mathrm{c}}. \tag{2.27}$$

Inserting Equations (2.26) and (2.27) into (2.25) gives

$$\frac{\kappa_\mathrm{e}\rho_\mathrm{c}}{\rho^2 c^2}\cos^2\theta_\mathrm{i} + \frac{\kappa_\mathrm{e}}{\rho_\mathrm{c} c^2}\sin^2\theta_\mathrm{i} = 1. \tag{2.28}$$

If the absorbing layer were given properties identical to the fluid medium from which the incoming wave is propagating (e.g. air), it is intuitive that there would be no reflections at the surface of the layer. Mathematically, this means that $\kappa_e = \rho c^2$ and $\rho_c = \rho$ and thus Equation (2.28) holds for all angles of incidence [5]. However, if the artificial absorbent is completely identical to the fluid, there is in practice no absorbing layer. The waves will unaffectedly propagate towards the model edges where they are reflected. Instead, consider a complex density $\rho_c = \rho_e - i\sigma/\omega$, where σ is the static flow resistivity of the layer. Equation (2.28) then reads:

$$\begin{aligned} &\frac{\kappa_e(\rho_e + i\sigma/\omega)}{\rho^2 c^2}\cos^2\theta_i + \frac{\kappa_e}{(\rho_e + i\sigma/\omega)c^2}\sin^2\theta_i = \\ &= \frac{\kappa_e(\rho_e + i\sigma/\omega)}{\rho^2 c^2}\cos^2\theta_i + \frac{\kappa_e(\rho_e - i\sigma/\omega)}{(\rho_e^2 + \sigma^2/\omega^2)c^2}\sin^2\theta_i = 1. \end{aligned} \tag{2.29}$$

For this equation to be satisfied approximately for all angles of incidence, the flow resistivity has to be small, so that $\sigma\rho/\omega << 1$ for all frequencies of interest [5]. To attenuate the sound throughout the layer, the flow resistivity should be linearly increased for each node when approaching the model edges. With suitable flow resistivity and if the artificial absorbers are thick enough, only negligibly small reflections will occur due to the approximation.

2.3 Urban Traffic Noise

Traffic noise is an especially large issue in urban areas, due to the vast amounts of people living in relatively small areas in close proximity to heavily trafficked streets. Also, due to the rapid expansion of today's cities, the demand for efficient acoustic solutions in order to make use of areas that have been previously considered less than habitable, such as previously industrialized areas or spaces close to larger roads and freeways, has increased.

2.3.1 Traffic Noise In Buildings

Depending on the source type, the effect on the receiving surroundings and the demands on the source itself can display a great deal of variation. Swedish Standard uses similar expressions for calculating the reduction index of a facade element with various traffic noise source types present, but with differently acquired sound pressure levels based on whether the noise source exists in the form of train, aircraft or road traffic [9].

According to Swedish Standard ISO 16283-3 [9], measurements of traffic noise propagating through an exterior wall can be performed with one receiver located close to the outside facade surface and one receiver on the inside. The reduction index for an exterior wall, $R'_{tr,s}$, when the sound source consists of traffic noise and the outside receiver position is placed in the facade of such a wall, is then estimated as

$$R'_{tr,s} = L_{1,s} - L_2 + 10 \log\left(\frac{S}{A}\right) - 3 \text{ dB}, \tag{2.30}$$

where $L_{1,s}$ is the sound pressure level in dB on the facade surface receiver position, L_2 is the sound pressure level in dB inside the receiver room (acquired through multiple receiver positions), S is the surface area in m^2 of the element through which the sound is transmitted and A is the equivalent absorption area in m^2 of the receiver room. The -3 dB term is a compensation for the reflection occurring at the facade.

Another method of calculating the reduction index is to view the dividing element, e.g. a facade, as a plate of infinite surface area, arbitrary thickness and a finite mass per area. In that case, the reduction index is obtained theoretically using the mass law, through the expression

$$R_0 = 10 \cdot \log\left(1 + \left(\frac{\omega m''}{2Z_0}\right)^2\right), \tag{2.31}$$

where ω is the angular frequency, while m'' denotes the mass per unit area of the wall and Z_0 is the characteristic impedance of air. This expression is useful for situations when a diffuse field on any side of the element is not necessarily present. With the assumption of a surrounding temperature of 20°C, the reduction index of the dividing element can be calculated in a simplified way [10]. Still viewing the element as an infinite plate with a finite mass and only considering normal wave incidence, R_0 is given by

$$R_0 = 20 \cdot \log\left(m'' f\right) - 42.5 \text{ dB}, \tag{2.32}$$

where the air temperature prompts the final term in the expression due to the insertion of the characteristic impedance of air at 20°C. Here, m'' is the mass per surface of the plate, while f is the frequency in Hz.

ISO 16283-3 also employs a variant of Sabine's formula that excludes the effect of air absorption and assumes an air temperature of 20° C to express A as

$$A \approx \frac{0.161V}{T}, \tag{2.33}$$

where V is the volume of the receiver room in m^3 and T is the reverberation time of the room in seconds. The main drawback of Sabine's formula though, is that it does not provide reliable reverberation time results for spaces with an average absorption coefficient above 0.3 [10]. Instead, the recommended formula for higher values of absorption is called Eyring's formula. It calculates the reverberation time as

$$T = \frac{55.26}{c_0} \cdot \frac{V}{-S \cdot \ln(1 - \overline{\alpha})}, \tag{2.34}$$

where c_0 is the speed of sound in air, V is the room volume, S is the total surface area of the room and $\overline{\alpha}$ is the average absorption coefficient of the room. Both Sabine's and Eyring's formulas require diffuse field conditions in order to be applicable. Such conditions can be assumed above the Schröder frequency, which, for a shoe-box-shaped room, is calculated as

$$f_{\mathrm{S}} = 2000\sqrt{\frac{T}{V}}, \tag{2.35}$$

using the same parameters T and V as in Equation (2.33) and (2.34) [10]. In 1965, Schröder's backwards integration, a method for determining the reverberation time in a room based on a measured decay of bandpass-filtered noise, was introduced [11]. According to Schröder, only one measurement is sufficient for estimating an average of infinitely many decay curves in the room, if this method is used [11]. During the measurement, the filtered noise shall be radiated in the room until a steady state condition is reached, whereafter the noise can be switched off. The signal $s(t)$ measured at the receiver position is then given by

$$s(t) = \int_{-\infty}^{0} n(\tau) r(t - \tau) d\tau \tag{2.36}$$

where $n(t)$ is the radiated noise, $r(t)$ is the impulse response of the noise filter, amplifiers, transducers and enclosure combined and τ is the time integral variable. The upper integral limit, $\tau = 0$, represents the time at which the noise is cut and $-\infty$ just clarifies that a steady state condition has been established during a sufficiently long time before switching off the noise. Further, Schröder [11] derives an expression for the squared signal, averaged over the ensemble of noise signals, arriving at the final expression

$$\langle s^2(t) \rangle = N \int_{t}^{(\infty)} r(u) du \tag{2.37}$$

commonly referred to as Schröder's backwards integration. Here, N is the noise power per unit bandwidth and the integration variable is given by the substitution $u = t - \tau$ [11]. After obtaining the decay curves from the backwards integration, the reverberation time can be calculated from straight line fits of the decay.

In the context of 3D FDTD modeling, the absorption area of the surfaces in a room or on a facade element can be considered in a similar fashion to the type of absorbing boundary conditions that were introduced in section 2.2.1. In reference to the explanation given there, ABCs are required to be quite wide in order for them to

completely absorb an incoming wave, while simultaneously possessing a sufficiently gently increasing flow resistivity that does not cause any major reflections. However, a deduction of a partially absorbing boundary can be made by considering a less resistant absorbing layer. Given sufficiently low size demands and a higher tolerance for partial reflections to occur, such a layer could be somewhat spatially efficiently placed in, for instance, a room and act as a porous absorber. The higher tolerance for reflections would also prompt the implementation of a uniformly resistive layer for a closer resemblance of an actual porous absorber. In reference to the claims in Section 2.2.1, a sufficiently high flow resistivity across the entirety of the absorber, let alone the end facing outwards from the wall, could potentially impose a large enough shift of impedance to cause such reflections.

2.3.2 Noise Barriers

When considering outdoor sound propagation, there are many external factors that increase the difficulty of that task. Beyond the usually quite simple model of a source, a receiver and a noise barrier are various atmospheric and physical effects that need to be taken into account when modeling real-life conditions. Attenborough et al. [12] attributed the total outdoor sound attenuation to a combination of contributions from geometric spreading of sound waves, atmospheric absorption and interference from surrounding objects and terrain. Examples of the latter category include ground and vegetation effects, as well as diffraction caused by obstacles that are either naturally occurring or deliberately placed for specific sound attenuation purposes.

Among the various phenomena affecting the propagation of sound in urban areas, diffraction around noise screens is a well documented subject, thereby prompting a set of various solutions for such problems. Most notable, according to Attenborough et al. [12], are the MacDonald solution for a thin half plane and the Hadden and Pierce solution for semi-infinite wedges. While the MacDonald solution does not take reflections off the face of the barrier into account, the Hadden and Pierce solution does, which is appropriate for studying barriers with finite impedance. The Hadden and Pierce solution also applies to thin screens when the wedge index, $v = \pi/\theta_r$, where θ_r is the angle between the wedge and the edge – receiver propagation path, is set to $v = 1/2$ [13][14]. Then, the total sound field is summarized in a single formula,

$$p_{\text{diff}} = \left(\frac{(1+i)}{2}\right)\left(\frac{e^{ikR'}}{4\pi R'}\right)\left(A_D(X_+) + A_D(X_-)\right) \tag{2.38}$$

which contains the diffraction integrals $A_D(X_-)$ and $A_D(X_+)$ [12].These are obtained by simplifying four diffracted wave terms that correspond to the propagation paths between source and screen, screen and receiver, as well as their respective images in the barrier. The wave terms are

$$\zeta_1 = |\theta_r - \theta_0| \tag{2.39}$$

$$\zeta_2 = 2\phi - |\theta_r - \theta_0| \tag{2.40}$$

$$\zeta_3 = \theta_r + \theta_0 \tag{2.41}$$

$$\zeta_4 = 2\phi - (\theta_r + \theta_0)\,, \tag{2.42}$$

where θ_r is the angle between the receiver side of the screen and the receiver to screen-edge propagation path, θ_0 is the angle between the receiver side of the screen and the source to screen-edge path, while ϕ is the angle between each side of a wedge when applicable. These expressions are used by Hadden and Pierce [13] to summarize each of their part of the total wave field. For the case of the thin hard screen, the wave field is simplified due to the wedge angle being small and expressed as Fresnel integrals, which are ultimately grouped into the compact formula in Equation (2.38).

By comparing the resulting sound pressure on the receiving side of the barrier to the pressure in the same receiver position with the barrier removed, the insertion loss for the hard screen, IL, could be determined as

$$IL = 20\log_{10}\left(\frac{p_{\text{without screen}}}{p_{\text{with screen}}}\right), \tag{2.43}$$

where $p_{\text{without screen}}$ and $p_{\text{with screen}}$ represent the sound pressure in the receiver position without and with a noise screen present, respectively [12]. Through some amount of derivation, some other effects subsequently become relevant in the case of a finite-mass screen. Similarly to the theory discussed in Section 2.3.1, a noise screen without acoustically hard properties is also subjected to transmission of the sound wave, governed by the reduction index of the screen, which ultimately would be expected to lower the total insertion loss of the screen.

3

Methods

The following sections present the code that was written and used to perform the simulations in this project, along with specific details of the models that were used. The extensions that were added to the previously mentioned 2D FDTD methods, in order to bring them into three-dimensional space, are also described in this chapter.

3.1 Code

The code that was written to conduct this study consisted largely of three main parts:

1. A base code, where the basic parameters used in the model were defined and the fundamental conditions of the simulation environment were established. This part also incorporated and adapted the theory from Section 2.1 into Matlab code.

2. A short pulse with a broad distribution of energy in the frequency domain, to simulate a sound source.

3. 2D visual representations of the tests performed in the model in the xy and yz planes.

The steps above were carried out in Matlab for a setting resembling an outdoor area, whose characteristics were those of a still medium with the option to implement a wind gradient. After constructing the model according to said steps, each part of the code was validated using analytical solutions and theoretical models.

3.1.1 Base Code

The foundational part of the code, referred to as the base code in this study, consisted of an implementation of the theory in section 2.1.1 covering spatial and temporal discretization of the pressure and velocity time derivatives. The base code specifically founded the basis for the non-moving medium with an optional wind gradient for conversion into a moving medium. Another required adjustment was that of the spatial and temporal discretization indexing used in Equations (2.7) – (2.10) and (2.11) – (2.16) for use in Matlab, in order to preserve the ratio between half-integer and integer indices whilst only consisting of integers.

3.1.2 Source Signal

The source signal, which was used to excite the various components of the model, was generated by implementing a delta pulse, filtered using an 8th order lowpass Butterworth filter with a cutoff frequency at 2000 Hz. Figure 3.1 shows the signal plotted in the time domain. For simplicity, the sound source was simulated as a monopole in a fixed position in the model. The amplitude of the signal was chosen arbitrarily and was easily scalable.

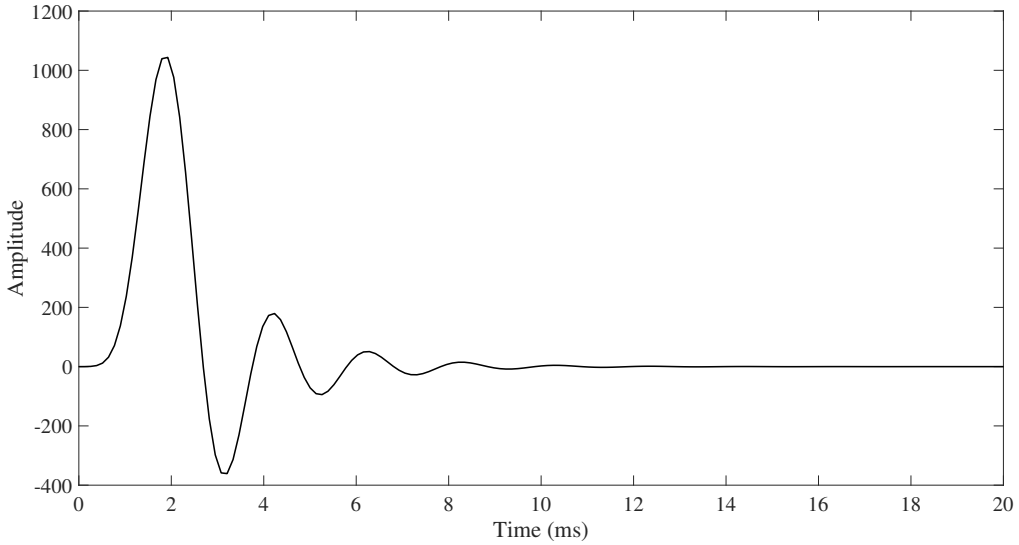

Figure 3.1: 2D time-domain plot of the source signal used for all tests in the study.

Mainly, the reason for specifically choosing a Butterworth filter was the need for a filter with a quick roll-off, in order to receive a stricter cutoff. As the quickness of the roll-off increases with the filter order, setting the order as high as 8 was advantageous and deemed sufficiently high by testing various filter orders. The tests also found that setting the cutoff frequency as low as 2000 Hz would ensure a minimal amount of near-zero magnitude components in the high end of the frequency spectrum, without being detrimental to the parts of the signal spectrum that were of interest. It also increased the clarity of the plots and decreased the amount of ringing after the source was switched off.

There was also the possibility to implement alternative source types in the model, that perhaps would have been more representative with regards to real-life traffic noise sources. These would for example include line sources and moving point sources, which are good approximations of either train passages and heavily trafficked roads or a single vehicle pass-by, respectively. While a line source is not excessively difficult to implement compared to a static point source, there are a few more steps to implementing a moving source in an FDTD model that were deemed too time consuming considering the time frame of the project. The amount of additional tests and simulations that the use of a line source implied eventually prompted the use of only a fixed point source as well.

3.1.3 Visualization And Implementation Of Sound Waves And Absorbing Boundaries

In order to visualize the sound levels produced by the source, the dimensions of the model region were categorized in two planes: one top-down view, showing the sound propagating in the xy plane, as well as one in the yz plane, that showed the scene from the side. The plots in Figure 3.2 are basic displays of the visual representation of the propagating sound waves in the model. The sound waves were assigned a colormap that displayed the pressure variations of the wavefronts.

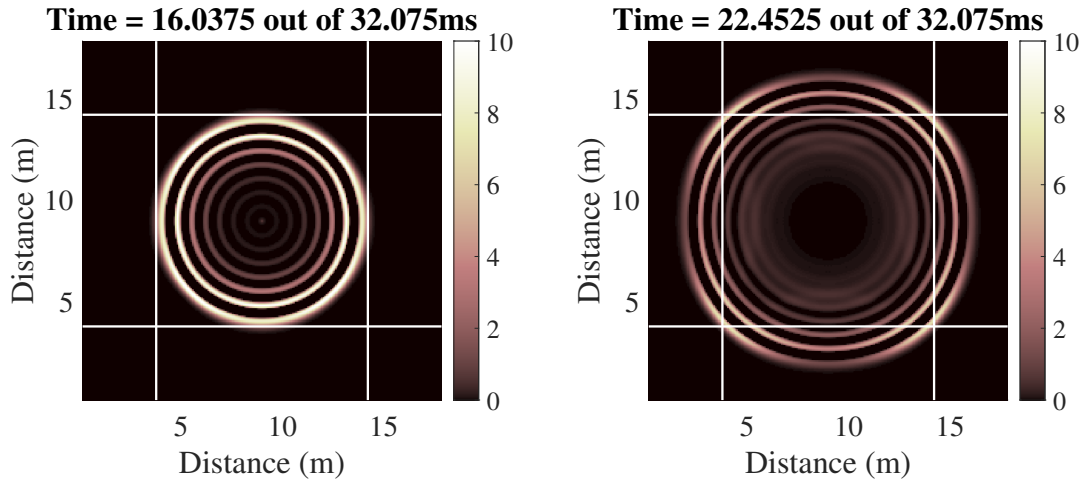

Figure 3.2: Visualization in the xy plane of the propagating sound waves at two separate instances in time.

In the figures, the waves fade out and are reduced in strength when reaching the absorbing boundary layers near the edges of the area, whose inner borders are marked using white lines. Ultimately, they are fully consumed as a consequence of the increasing flow resistivity in the layers. The strength and width of the boundary layers determine the location and the effectiveness of where the waves begin to fade out. For the simulations performed in this study, a surrounding boundary with the thickness of 30 to 40 nodes, along with a flow resistivity of $1 < \sigma < 3000$ raylm^{-1}, was used. The upper boundary of the flow resistivity range was deemed sufficiently large to eventually absorb the majority of the incident waves, while the lower boundary was set small enough to not cause any immediate reflections due to the sensation of an impedance change.

3.2 Numerical Validation

To ensure that the code was properly representing the phenomena that were modeled, a series of validation tests were performed using analytical models of the situations simulated in the model. The following section presents those tests and describes how they were implemented. For all FDTD simulations executed for validation, the grid spacing was set to 75.6 mm, which is 1/15 of a wavelength at 300 Hz. Since traffic in urban areas mainly causes high sound pressure levels at low frequencies and since the low frequencies generally dominate the traffic noise transmitted into buildings, the lower-to-mid end of the frequency range was considered the most interesting for this particular study. The Courant number was set to 1 in the non-moving medium simulated in all tests, resulting in a temporal step size of 0.13 ms.

3.2.1 Rigid Screen

An acoustically hard noise barrier was modeled using FDTD and compared to the properties of an actual hard screen through two separate tests. To test its reflective capabilities, a hard screen of infinite height was used to verify that the implementation of such a screen would constitute a perfectly reflective surface in the model. Additionally, a resolute parameter for comparing the effect of a finite-height screen to an analytically calculated counterpart was required. Therefore, the insertion loss of the screen was calculated using Equation (2.43) and compared to the insertion loss calculated from the theory in Section 2.3.2.

To verify that the hard wall was perfectly reflective, the reflected sound wave was compared to a wave propagating in free-field. The source was placed between the wall and the receiver, 3 meters in the normal direction from the wall and 1 meter from the receiver location, resulting in a total propagation distance of 7 meters. The free-field simulation was executed accordingly, with the receiver placed 7 meters from the source, as can be seen in Figure 3.3.

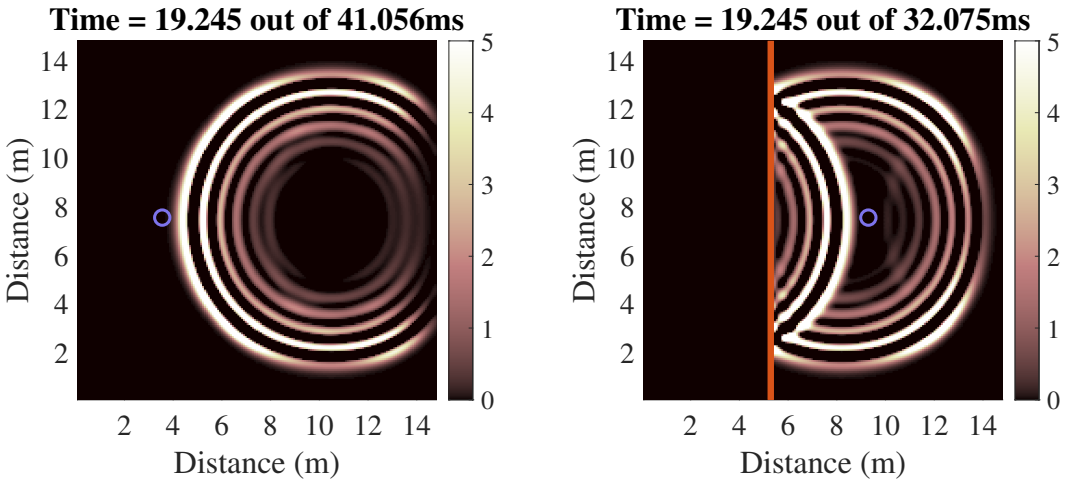

Figure 3.3: Visualization in the xy plane of a reflection at a rigid screen without absorption (a) and with a layer of absorption with the thickness of 6 nodes (b).

The propagation paths of the wavefronts in the two cases seen in Figure 3.3, between the receiver and the source positions, were equally long. Thereby, if the wave reflected at the surface was identical in strength to the direct wavefront in the free-field when reaching the receiver position, the wall would be confirmed to be perfectly reflective.

To account for other effects and parameters such as diffraction and scattering, a noise screen of finite height was needed. Therefore, In Figure 3.4, the effect of a rigid, 3 m high noise screen is demonstrated. This test consisted of two separate simulations. First, a receiver and a source were placed at a distance of 5.5 m apart. Then, a rigid noise barrier with a height of 3 m was placed between the two positions, 3.5 m from the source and 2 m from the receiver, blocking their intermediate line of sight.

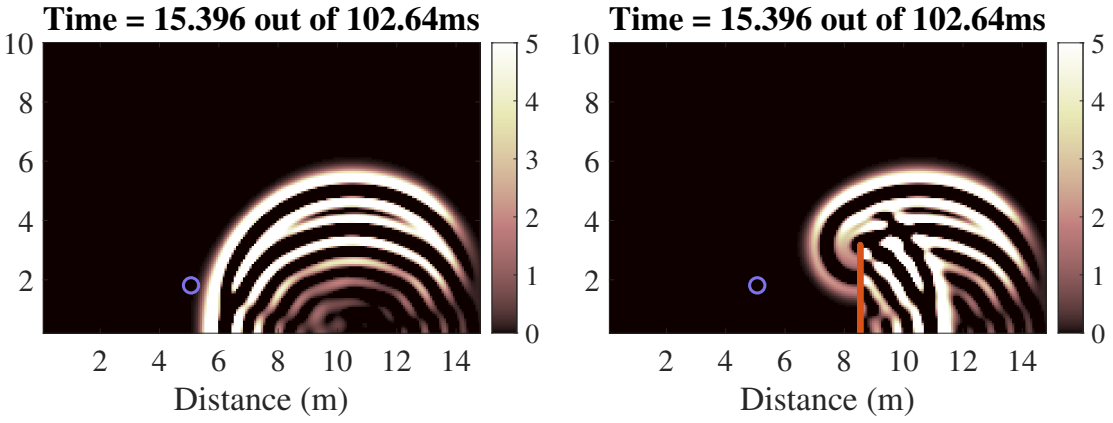

Figure 3.4: Visualization in the yz plane of the propagating sound waves without (a) and with (b) a rigid noise screen.

The receiver position that was used to estimate the insertion loss of the screen is marked with a blue circle in Figure 3.4. The noise screen is displayed in Figure 3.4 (b) as a red bar. Judging by the color of the wavefront in both cases, the sound pressure was considerably lower near the receiver position when the screen was implemented. The noise screen modeled in FDTD could then be validated by comparing its effects to the results of an analytically calculated screen model that utilized the Hadden-Pierce solution for sound diffraction around a wedge [13], summarized in Section 2.3.2.

3.2.2 Screen With Finite Surface Mass

A single wall with the thickness of one grid element, covering one entire yz plane and with a surface mass of 50 kg/m^2, was constructed. To verify that the mass law was valid for the FDTD model, the pressure was measured at the receiver location with and without a separating screen, both cases displayed in Figure 3.5.

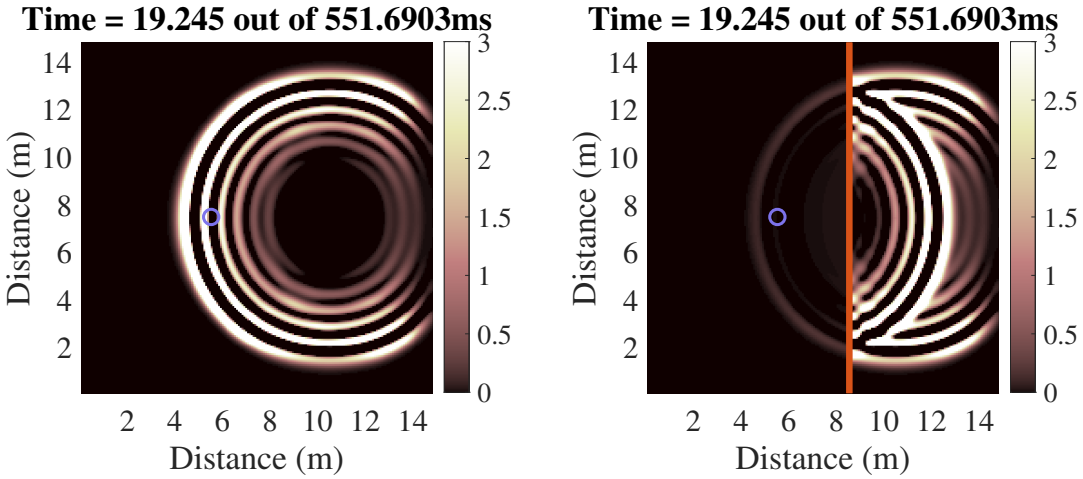

Figure 3.5: Visualization in the xy plane of mass law validation test, with the wave-front propagating in free-field on the left and transmitted through a wall with finite mass.

Theoretical values of the reduction index were calculated according to the mass law Equations (2.32) and (2.31). By inserting these reduction indices into Equation (2.30), analytical, expected, values of L_2 could be compared to the numerical value obtained from the simulation. The -3 dB term was eliminated since L_1 was measured in free-field and since no reflections occurred at the receiver side of the wall, the term $10\log(S/A)$ was also excluded. Hence, the Equation could be written as $R_0 = L_{1,s} - L_2$.

Figure 3.6 demonstrates the implementation of a noise screen with a surface mass of 15 kg/m^2. The figure depicts sound propagation against the screen at two separate instances in time. Compared to the rigid screen case, the sound at the receiver now has additional energy due to transmission through the noise barrier.

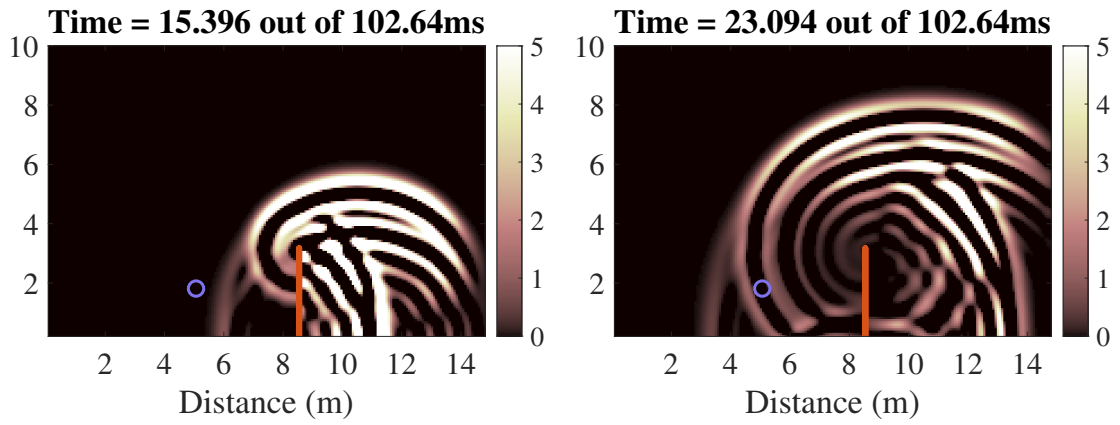

Figure 3.6: Visualization in the yz plane of the propagating sound waves over a finite-mass screen at two separate instances in time.

In the earlier instance of the sound propagation demonstrated in Figure 3.6 (left), a transmitted wave is clearly visible as a partially faded wave on the receiver side of the screen. The receiver location is marked by a blue circle, situated in a position which is influenced by both transmitted and diffracted sound waves for the finite-mass case. If the mass of the screen is increased, the transmission through the screen is expected to decrease. For sufficiently high values of mass per area of the screen, it can eventually be considered an acoustically hard object.

To validate the effect of the finite-mass screen, simulations were executed with a hard screen setup of identical geometry compared to the previous test, as well as an infinitely high screen with the surface mass 15 kg/m^2, as shown in Figure 3.7.

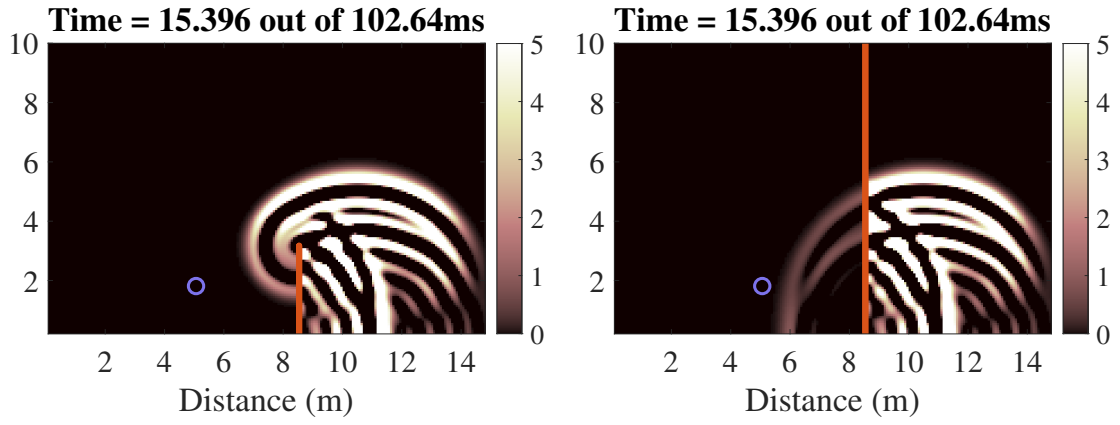

Figure 3.7: Visualization in the yz plane of sound propagation over a hard, finite-height noise screen (left) and an infinitely high, finite-mass screen (right).

Comparing the visualization on the left in Figure 3.7 to the earlier instance of the simulation shown in Figure 3.6, the transmitted sound wave constitutes the only discernible difference between the two snapshots. Another visible transmitted wave appears to the right in Figure 3.7, seemingly subjected to equal amounts of attenuation as the transmitted wave in Figure 3.6 (left). Summing up the energy from the two cases presented in the figure above should give an indication of the effect of the finite-mass noise screen in Figure 3.6. The energy summation is however made under the assumption that the diffracted waves in Figure 3.6 (left) and the transmitted waves in Figure 3.6 (right) are uncorrelated, which does not correspond to the investigated case.

3.2.3 Absorbing Layers As Room Absorbers

By placing a sound source in front of an acoustically hard wall, the strength of the direct sound and the reflected sound in the normal direction of the wall could be compared in a receiver position placed a distance further from the wall, in line with the source. An absorbing layer was designed in the same way as the absorbing boundaries of the model, using a successively increasing flow resistivity and placed in front of the hard wall. This allowed partially absorbed sound waves to reach the receiver position and thus be compared to their fully reflected counterparts. The resulting ratio between the fully and partially reflected waves determined the absorption coefficient of the combined wall and absorbing layer.

Figure 3.8 shows the reflective properties of an acoustically hard screen, compared to a case where an absorbing layer has been placed in front the screen. In the figure, the screen is symbolized by a red bar, while the absorbing layer is displayed as a thicker, green bar. The source was placed between the screen and receiver, with a distance of 3 meter to the screen and 1.5 m to the receiver. As seen in the figure below, the distance between source and screen was sufficient to make the direct wavefront pass by before the reflected sound reached the receiver position.

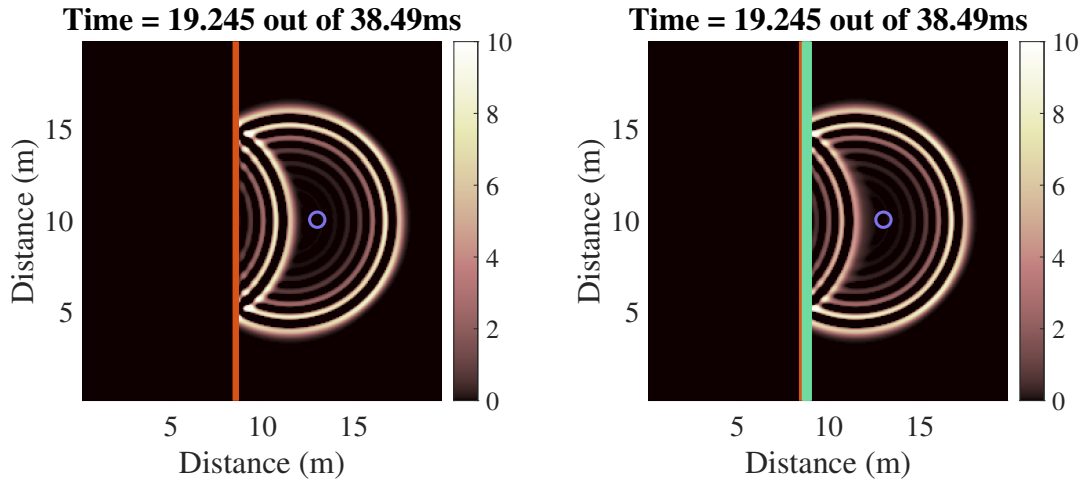

Figure 3.8: Visualization (xy plane) of a reflection at a rigid screen without absorption (a) and with a layer of absorption with the thickness of 6 nodes (b).

The effect of inserting an absorbing layer can be seen in Figure 3.8 (right), where the reflected sound wave is notably weaker compared to the reflection in Figure 3.8 (left). The sound pressure in the reflected wave for the respective cases was analyzed to allow for separation of the fully reflected wave and the partially reflected wave from the direct wave, in order to deduce the effect of the absorbing layer. The absorption coefficient was then used to analytically estimate the reverberation time for the forthcoming receiver room validation, using Equations (2.33) and (2.34).

As an alternative to the previously mentioned absorbing layers, the effect of modeling absorbing layers with constant flow resistivity throughout the layer was also considered for this study. Many porous absorbers are homogeneous in both material and geometry, which would imply that applying the same amount of resistivity to every point in the entire layer could be an accurate representation of an actual absorber. However, after undergoing the same tests as the layers with increasing flow resistivity did, the results for the constantly resistant layers proved to be less accurate than the layers with increasing flow resistivity when compared to the corresponding analytical models. Therefore, further investigation of such layers was deemed redundant and, as an additional part of the study, too tedious regarding the time frame of the project.

3.2.4 Receiver Room

The following simulations consisted of calculating the reverberation time in a room, as well as the sound level difference between the inside and outside of the room induced by a separating facade element. A 4 m $\times$ 6 m $\times$ 3 m enclosure was designed to simulate a receiver room. The wall facing the source was modeled as a mass while the remaining walls were rigid, with the intention of only having transmission through the separating wall during the level difference measurements. Under real-life conditions, small parts of the sound is transmitted via the receiving room to its surrounding spaces in the building. However, the transmitted energy is in general negligibly small compared to the absorbed and reflected energy inside the receiving room. Figure 3.9 presents two snapshots of the simulation, captured at two separate instances in time.

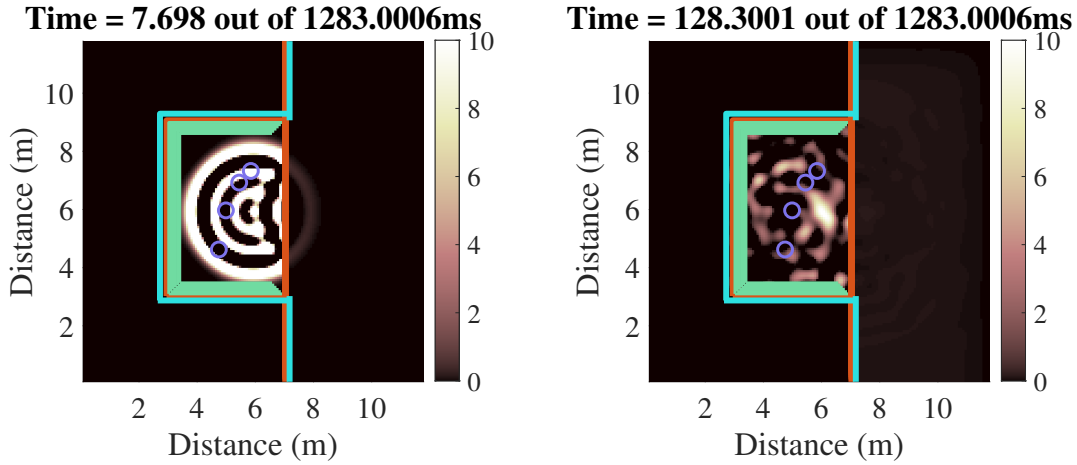

Figure 3.9: Reverberation time measurement (xy plane) with the sound source positioned inside the receiver room, along with multiple receiver positions.

The sound source was first placed inside the room for reverberation time calculations. The left hand image in Figure 3.9 depicts the simulation at an early instance in time, shortly after exciting the source. Here, the placement of said source can also be distinguished, as well as the receiver positions between which the reverberation time was averaged. At a later point, the sound pressure is significantly reduced due to absorption, as seen in the visualization to the right. The red bars represent the walls of the room and the green bars symbolize the absorbing layers. A substantial amount of leakage occurring in the junctions between the hard walls of the room and the facade was observed in the initial tests. The leakage was believed to be caused by the placement of the wall intersections relative to the half-integer spacing in the pressure and velocity grids. In order to prevent the measurement results from being distorted, the hard parts of the facade were reinforced by an additional layer of hard walls that overlapped the leaking junctions. The reinforcements are represented by the light blue lines.

After obtaining the results of the FDTD simulation, decay curves in 1/3rd octave bands were calculated through Schröder's backwards integration in Equation (2.37), and the reverberation time was calculated from straight line estimations of the curves, as shown in Figure 3.10. The reverberation time could be used for validation of the absorbing layer.

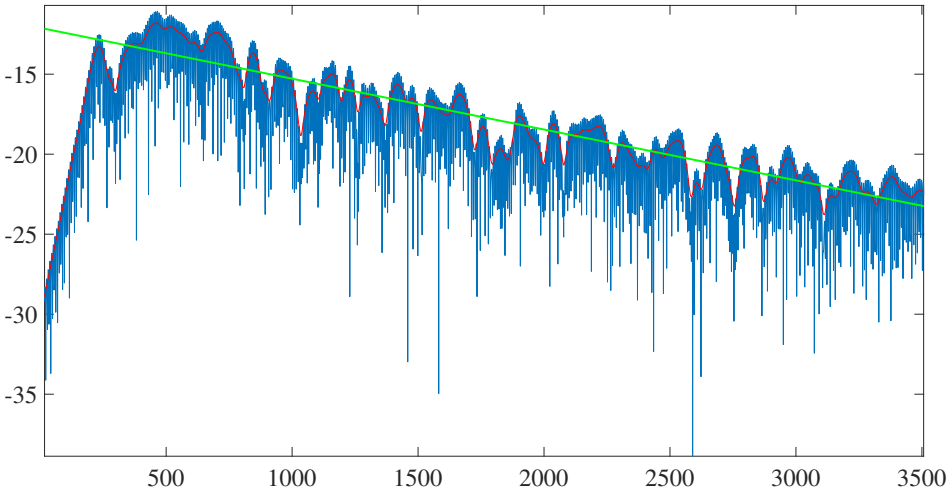

Figure 3.10: Example of straight line fit to the decay, represented by the green line.

Once the reverberation time of the room had been calculated, a test to validate the sound insulation of the facade could be performed. By moving the source outside of the room, the resulting level inside of the room after the sound had been transmitted through the facade could be compared to free-field levels at an equal distance from the source. The setup used in this test can be seen in Figure 3.11.

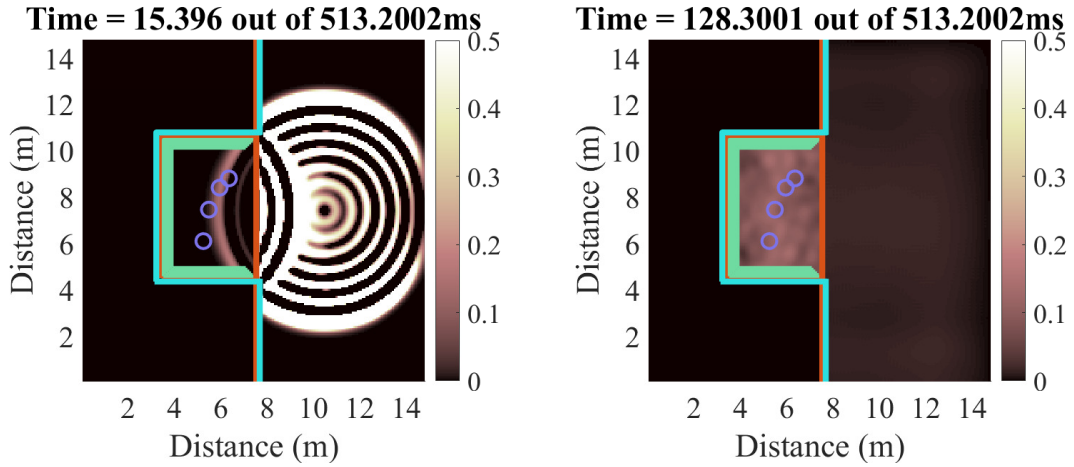

Figure 3.11: Level difference measurement (xy plane) with the sound source positioned outside the receiver room.

In Figure 3.11, the blue circles represent the receiver positions in the room, which were randomly placed within the nearest boundaries of the absorbing layers and the facade element. There, a total simulation time of over 0.5 s was chosen in an attempt to capture the entire impulse response of the room. Similarly to the test in Figure 3.9, two instances in time were picked to visualize examples of various stages of the decay in sound pressure inside of the room, as seen in Figure 3.11. Out of this test, sound pressure levels could be extracted from the receiver positions inside of the room. These were then compared to free-field measurements using the same source and receiver positions, in order to distinguish the exact effect the room had on reducing the sound pressure.

4

Results

This section provides the results of the simulations and tests that were carried out throughout the study. The results that were deemed useful and relevant were those obtained from the validation tests conducted using the absorptive elements in the receiver room, as well as the transmissive facade element and the noise screen when both were modeled with a finite surface mass.

4.1 Hard Screen – Infinite Height

The results of the tests involving an infinitely high rigid screen, which was described in section 3.2.1, are presented in Figure 4.1, as time signals of the respective cases.

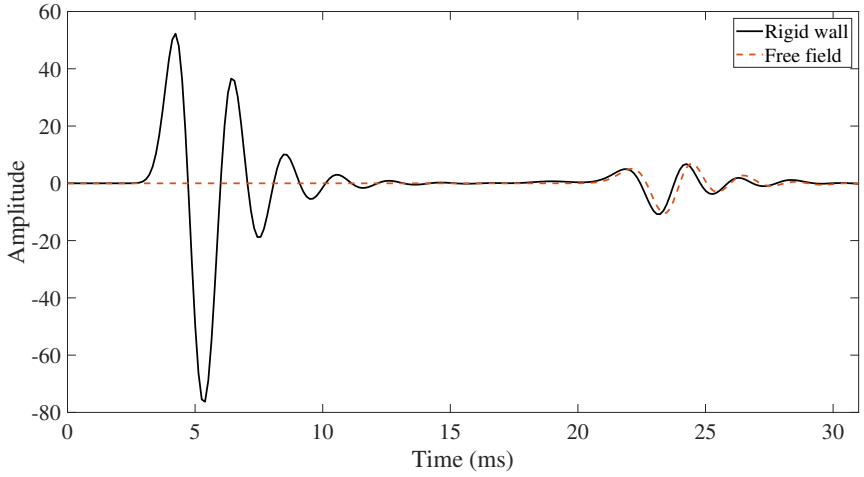

Figure 4.1: Amplitude of a wave propagating in free-field and after being reflected off a hard screen. The solid line describes the time signal of the reflected wave, while the dashed line represents the time signal of the wave propagating in free-field.

The first deviation from 0, at around 3 ms, is the direct wave reaching the receiver position on the source side of the wall. The second deviation, which occurs after 20 ms, is the direct wave reaching the receiver in the free-field case and the reflection from the hard wall reaching the previously mentioned source side receiver. There is

a slight difference in the time of arrival between the two cases, which is likely caused by round-off errors when converting distances in meters into nodes. For the free-field case, the wave seems to propagate a distance of one additional node compared to the reflected wave in the rigid wall case, before reaching the receiver. This deviation, however, is not large enough to cause any notable differences in the forthcoming results.

Figure 4.2 compares the sound pressure levels of the aforementioned case in the frequency domain. The results are presented in narrowbands.

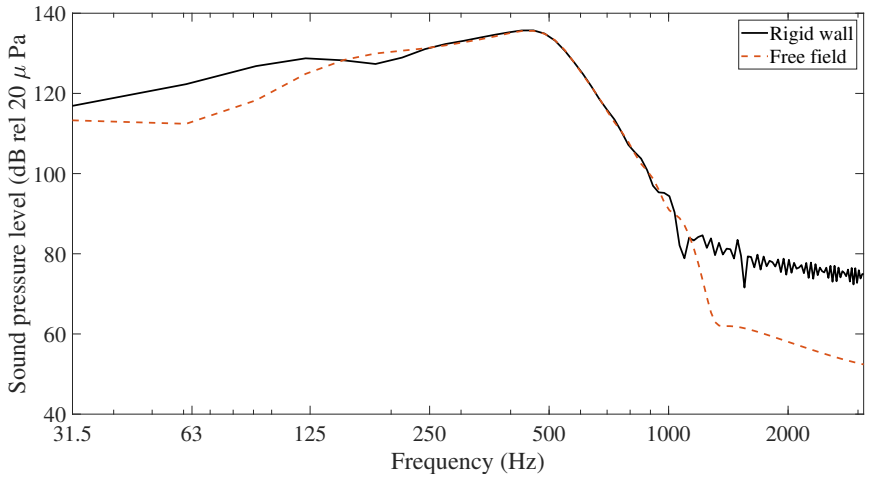

Figure 4.2: Sound pressure levels of the free-field and the reflected case in the frequency domain. The solid line represents the case of the hard wall reflection, while the free-field levels are plotted using the dashed line.

For a perfectly reflecting wall, the direct sound in the free-field and the reflected wave should be equal in magnitude. In nearly the entirety of the frequency where the results of the FDTD model are valid, the levels of the two cases are almost identical. It is only above about 1000 Hz that the curves level out, but around 20 dB apart. Judging from the shape and level of the reflected case, reflected high frequency content seemingly becomes unstable in the FDTD model.

The figure also shows some greater deviations in the low end of the frequency range, between about 31.5 and 250 Hz. Here, the deviation is at its largest near 63 Hz, with a level difference of 6 dB. Only a short time interval between about 20 and 30 ms, corresponding to 115 time steps, was converted into the frequency domain for this test. By using so few data points for the conversion, the frequency resolution becomes quite low. Between 30 and 250 Hz, there are only six points in which the sound pressure level has been evaluated, which could be the reason for the relatively large level deviations in that range.

4.2 Hard Screen – Finite Height

Figure 4.3 compares the impulse response from the FDTD simulations and the insertion loss for a 3 m high, rigid screen calculated through both FDTD and the Hadden-Pierce solution. The source was located 0.6 m above ground, at a horizontal distance of 2 meters from the rigid noise barrier. On the other side of the screen, the receiver was located 1.6 m above ground and 3 m from the reflective screen. This simulation was executed in 800 time steps.

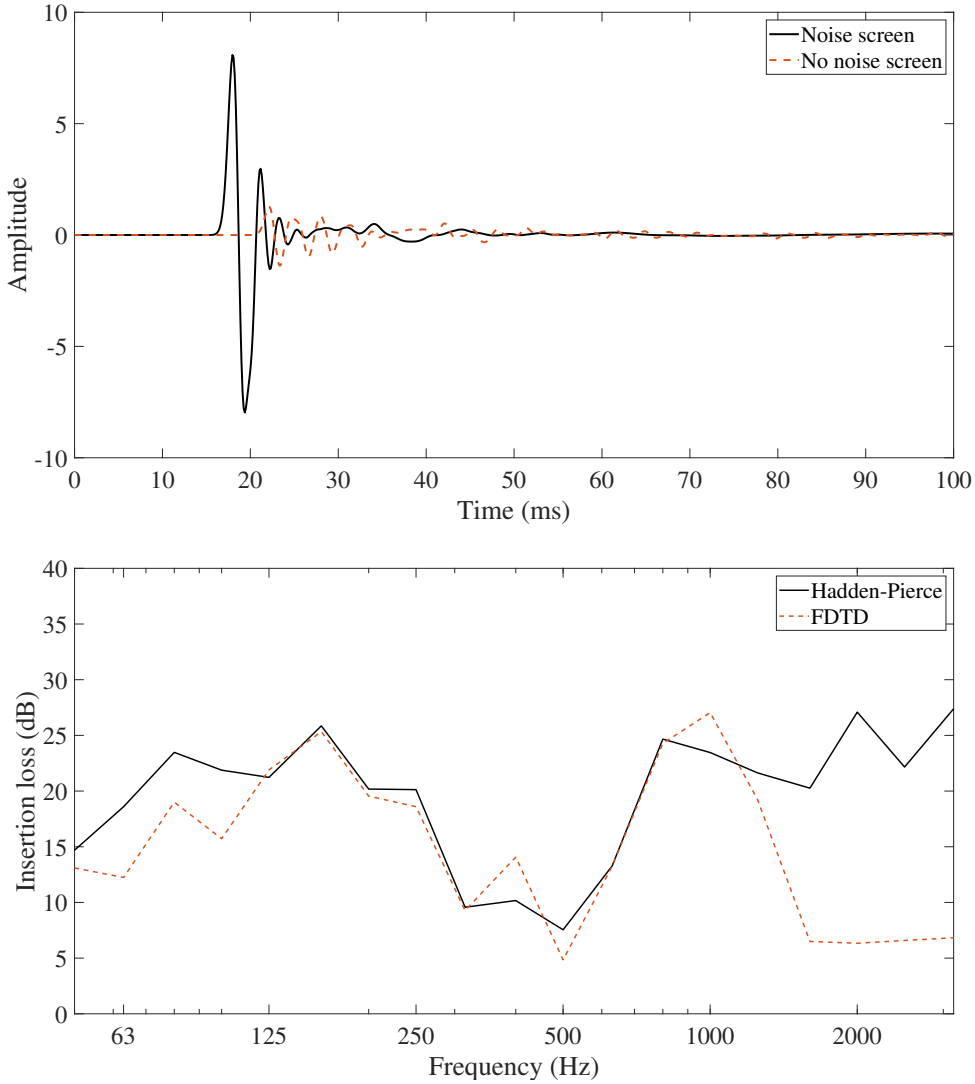

Figure 4.3: Impulse response for the case without and with screen (top) and insertion loss in 1/3rd octave bands calculated through the Hadden-Pierce method and compared to FDTD (bottom).

Due to the longer path between source and receiver, the impulse response for the case with the screen inserted is delayed relative to the case without screen. It can

further be seen in 4.3 (top) that the impulse response is smeared out due to the sound wave being subjected to several reflections within the edges of the screen, causing a prolonged radiation sequence at the top of the screen. Phenomena such as reflections, diffraction and scattering work as expected up to about 1000 Hz. From that point on, the curves start to deviate significantly, seen in Figure 4.3 (bottom). The wavelength at 1000 Hz is 0.34 m which is only about 6 times the grid spacing used for the simulation. As mentioned in Section 2.1.3, the spatial step size should only be a small part of a wavelength of the highest frequency of interest for sufficient resolution. Otherwise, the general trend is correct for the FDTD solution, in the sense that the insertion loss increases with frequency. Around 250-500 Hz, interference between the ground reflections and the direct wave causes the curves to dip. Interference in this part of the range could have been avoided by placing the source closer to the ground to shift the interference higher in the frequency range.

In the range 125-800 Hz the curves follow each other closely, except at the 315 Hz 1/3rd octave band where the insertion loss is about 4 dB higher for the FDTD calculations compared to the Hadden-Pierce solution. The deviations varied depending on the number of time steps used for the FDTD simulation. Mainly, the reason for this is probably small reflections at the absorbing boundaries, which could also explain the more distinct deviations at low frequencies. Further, the number of time steps used was insufficient for the sound to fade out entirely. Longer simulation times would have allowed a large enough time frame for the sound pressure to reach zero, but also provided enough data points for sufficiently high spectral resolution when converting to the frequency domain.

4.3 Finite-Mass Screen

For the case of the finite-mass screen, the resulting quantities that were considered were the sound pressure levels in the receiver positions in front of and behind the screen, along with the insertion loss of the screen. The levels obtained from the FDTD simulation were compared to analytically calculated levels. Figure 4.4 shows a comparison between the results of the FDTD calculations and the analytically determined sound pressure levels.

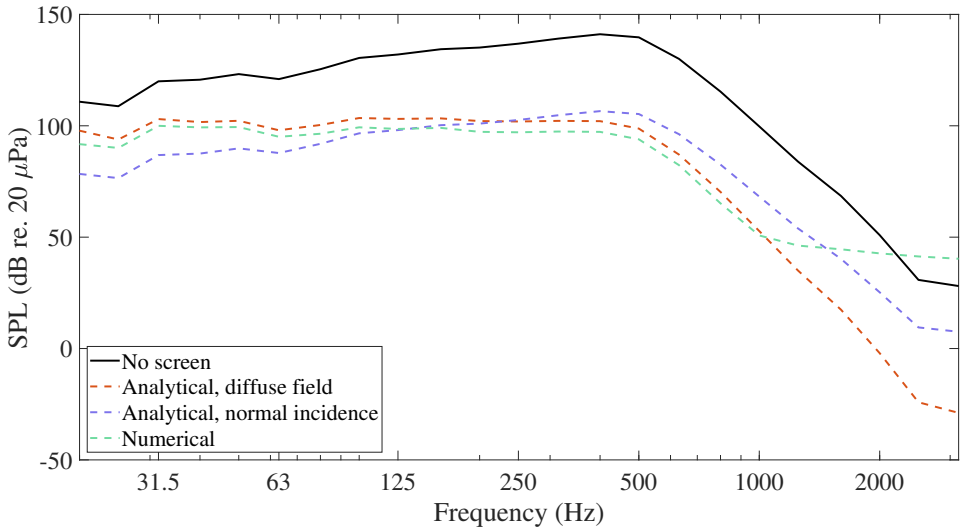

Figure 4.4: Sound pressure levels in a receiver position in free-field, compared to the levels in the same position after implementing a screen with 50 kg/m^2 of infinite height

In Figure 4.4, the dashed lines represent the numerically and analytically calculated values of the sound pressure level in a position behind a finite-mass screen, while the solid line shows the level in the same position when the screen is removed. The red line is calculated from Equation (2.32) and (2.30) and the blue line from (2.31) and (2.30). The numerically calculated values coincide well with the analytical results up to about 900 Hz, where the energy levels out and remains almost constant for the rest of the frequency range. While the free-field wave-front has a continuous behaviour up to about 2.5 kHz, the numerically calculated transmitted sound pressure level is even higher than the free-field value above 2000 Hz.

Since the red line is obtained from diffuse-field calculations, it would have been expected that the numerical results rather followed the blue line which represent transmission through an infinite wall and for normal incidence. However, the tendency of a sound pressure level decreasing with frequency relative to the free-field value is very typical and the curves are in general well correlated, which indicates that the numerical results are valid up to about 1000 Hz.

In Figure 4.6, the sound pressure level behind a 3 m high finite-mass screen with a surface mass of 15 kg/m^2 is compared to that of the acoustically hard screen validated in the previous section. These tests were performed using the setups shown in Sections 3.2.1 and 3.2.2, for finite-height noise barriers. The dashed line represents the expected result, obtained through energy summation of the diffracted wave from the rigid, 3 m high wall and an transmitted wave through the infinitely high wall with a surface mass of 15 kg/m^2 shown earlier in Figure 3.7.

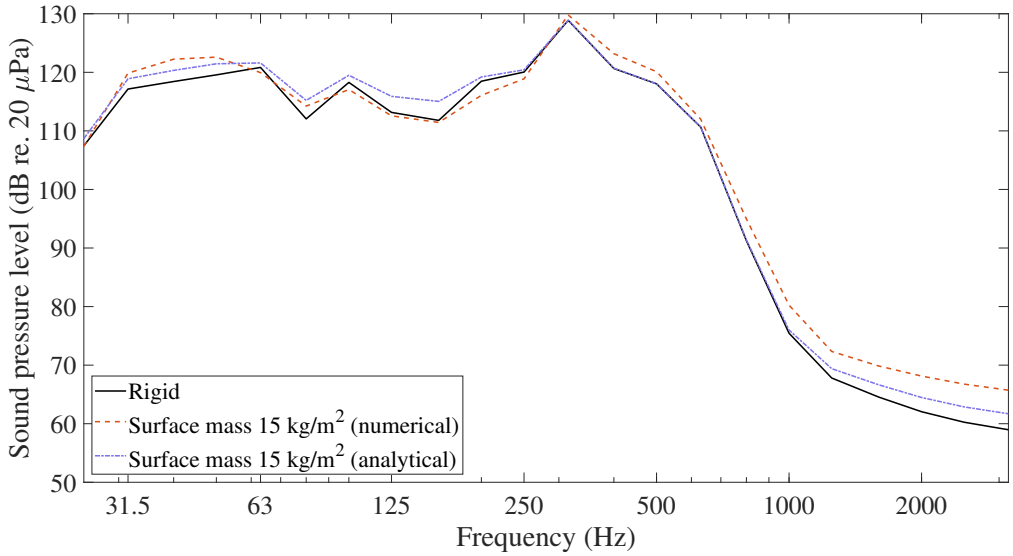

Figure 4.5: Sound pressure level for the case with rigid and with finite-mass screen.

A surface mass of 15 kg/m^2 is commonly used for noise screens. Between 80 and 250 Hz, the sound is actually softer for the case with the finite-mass screen, which could be due to destructive interference between the transmitted and diffracted waves. The analytical solution does not take interference into consideration, since the energy summation assumes that the sources are uncorrelated. Past 1000 Hz, the numerically determined curve of the finite-mass screen levels out at around 10 dB above the rigid screen, while the analytically calculated values are slightly more coincident with those obtained for the rigid screen. The curves are expected to deviate trend-wise in that area though, since the range above 1000 Hz has been established as unable to provide reliable results earlier on in the study.

The insertion loss of the hard screen, as seen in Figure 4.3, was also used to analyze the performance of the finite-mass screen. In Figure 4.6, the results of both analytical and numerical calculations of the finite-mass screen insertion loss are compared to the same parameter for the hard screen.

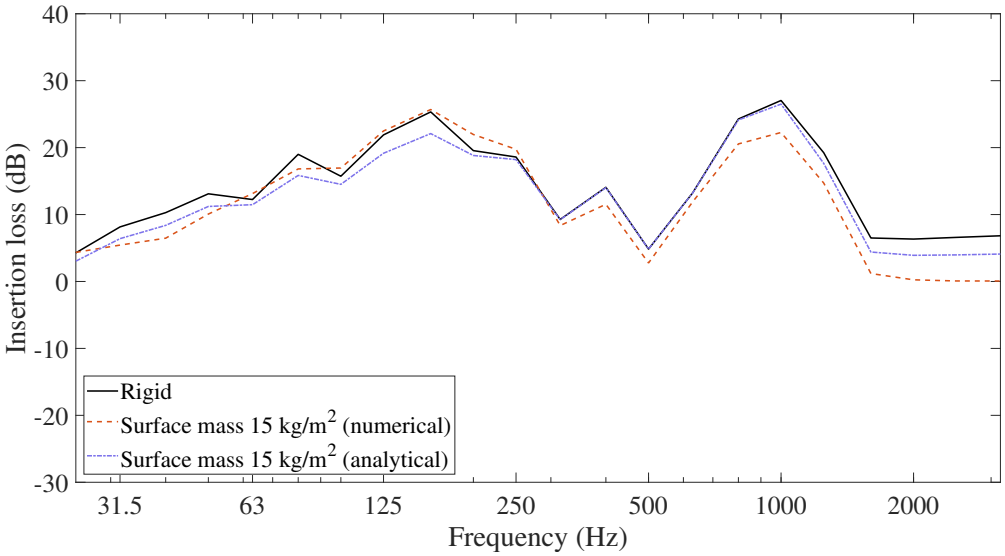

Figure 4.6: Insertion loss for the case with rigid and with finite-mass screen.

In the figure, the insertion loss of each screen is generally at its lowest in the low end of the frequency range. There, the general trend of the results behave as expected, in the the sense that the insertion loss increases by frequency. In the region around 250 to 500 Hz, however, that trend is broken for both curves. There, they both exhibit especially low values due to interference between the direct sound and ground reflections, as previously discussed in connection to the insertion loss curves in Figure 4.3.

4.4 Absorbing Layers

This section presents and discusses the results of the tests described in Section 3.2.3, where an absorbing layer was placed in front of a hard wall next to a sound source. Here, the respective time signals of the reflected waves, as well as the absorption coefficients for various amounts of flow resistivity in the absorbing layer, are displayed and compared. Starting with the time signals, Figure 4.7 shows the time domain representation of a sound wave reflected towards a rigid wall onto which the artificial absorbers under investigation were attached. The early pulse between 5 and 15 ms is the direct wavefront. The highlighted zone marks the reflected waves, where the amplitudes start deviating depending on their amount of flow resistivity.

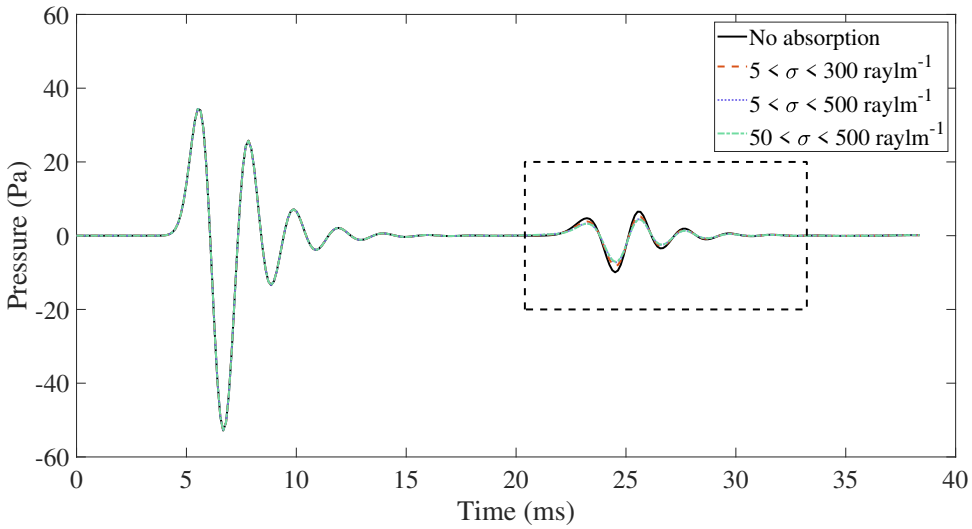

Figure 4.7: Time domain signal without absorption and with various absorbing layers attached to the rigid surface.

Upon inspection, a visible decrease in amplitude for the reflected wave for the cases where absorption has been applied can be noted. In order to specifically study the reflected waves themselves, Figure 4.8 provides a detailed view of that part of the time domain function. The time limits of the detailed case were chosen such that the direct wave had enough time to more or less completely fade out, as well as to let the reflected wave be reduced to zero.

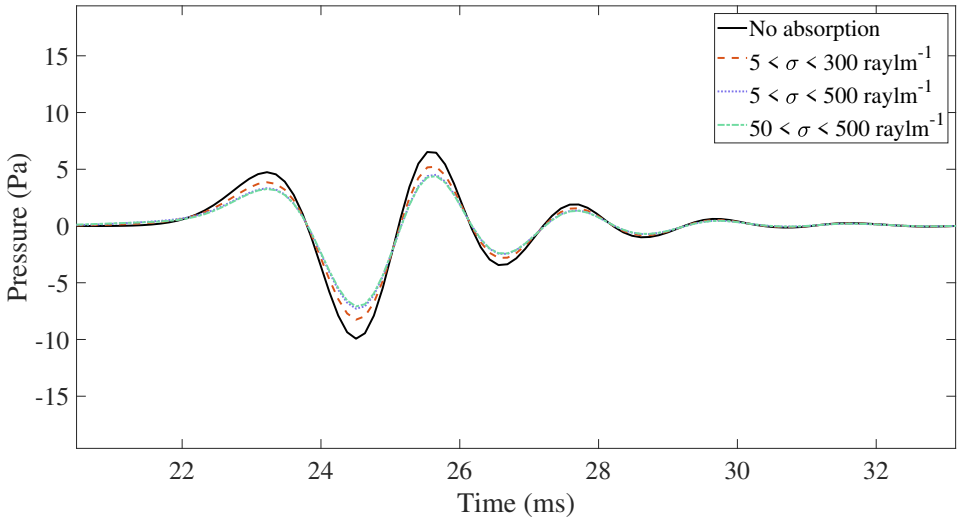

Figure 4.8: The reflected sound wave with varying amplitude due to different degrees of absorption between each case.

By studying the reflected wave closely, the effect of the absorption on the rigid wall becomes apparent. Figure 4.8 shows a clear decrease in amplitude for the cases with added absorption, when compared to the reflection from the rigid wall. The most distinct effect on the absorbing cases seems to stem from increasing the maximum flow resistivity in the far end of the absorbing layer. However, a slight decrease in magnitude can also be identified between the cases where the flow resistivity in the low end of the absorbing layer differs. This result confirms that absorption actually occurs in the layer and suggests the specific degree of sound pressure level attenuation caused by a certain amount and configuration of flow resistivity.

The loss in sound pressure level was calculated for the different reflective cases in the frequency domain. In Figure 4.9, the amounts of loss obtained between the varying degrees of flow resistivity in the absorbing layer compared to the fully reflective case are displayed in 3rd octave bands. In this case, the effect of varying both the upper and lower limits of the absorbing layer was studied.

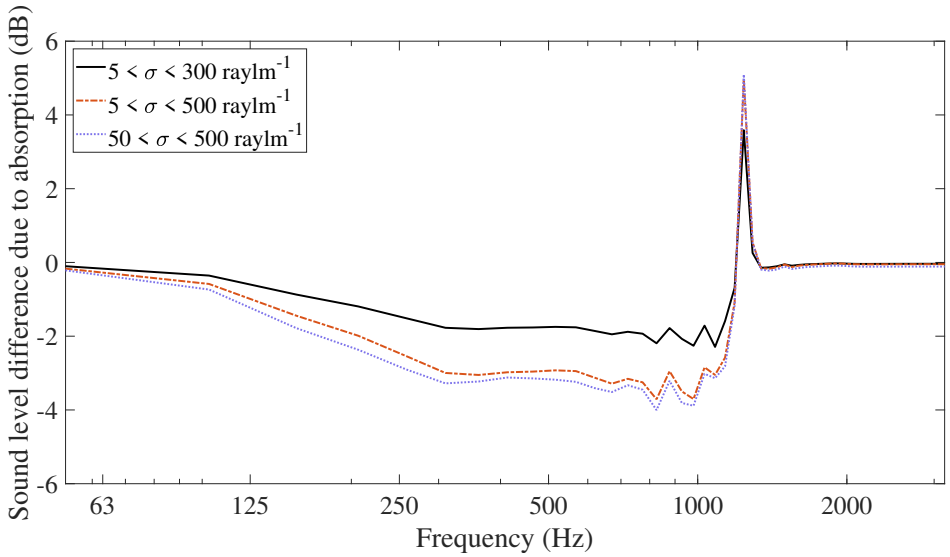

Figure 4.9: Difference in sound pressure level due to absorption relative to the case without absorption.

In the lower end of the frequency range of interest, the loss due to absorption is almost zero for all absorbers. In order to have greater low frequency attenuation, thicker layers or a separating gap between the layers and the wall would have been needed. Low attenuation in the lower frequency range is however typical for porous absorbers. The effect of the absorbers increases with frequency until about 300 Hz where the curve flattens out. Fluctuations are observed between 800 and 1000 Hz and it can again be stated that frequencies beyond 1000 Hz are outside the valid range for the simulations in this study.

Several further tests are needed to draw conclusions on the effect of changing the flow resistivity and to be able to control the absorption characteristics of absorbing layers.

Based on these results, however, increasing the lower end of the flow resistivity range in the absorbing layer has quite a small effect on the sound pressure level compared to changing the high end. The absorption coefficients corresponding to each case can be seen in Figure 4.10

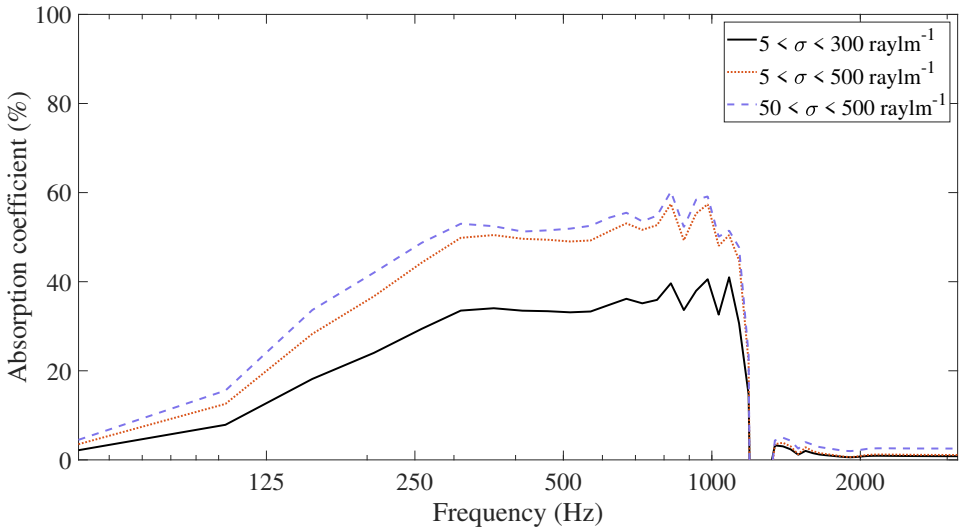

Figure 4.10: Absorption coefficients for the three absorbing layers with various flow resistivities, all with thickness of 6 elements.

The absorption ratio increases with frequency with only a few dips and peaks deviating from the general tendencies. From these results, the expected reverberation time of the receiver room was calculated through Sabine's formula. If thick absorbing layers are suitable for room absorption usage in FDTD models, the analytically and the numerically obtained reverberation time should match well. The results are compared in Section 4.5 where the absorbers will be discussed further.

4.5 Receiver Room

After performing calculations for the receiver room, the parameters deemed the most interesting to analyze were the reverberation time of the room and the resulting sound pressure level difference between free-field and the case with the facade separating the outdoor sound source and inside receiver positions. These tests were conducted using the most relevant amount of increasing flow resistivity in the absorbing layers.

4.5.1 Reverberation Time

Figure 4.11 displays the reverberation time in the receiving room in third-octave bands. The Schröder frequency of the room, determined through Equation 2.35, is ~ 120 Hz. For efficiency, the layer with the highest amount of absorption ($5 < \sigma <$

500 raylm^{-1}) from the absorber tests was used in order to minimize the number of time samples needed to obtain reliable reverberation time results. The layer covered every surface except for the facade facing the source, as shown in Figure 3.9.

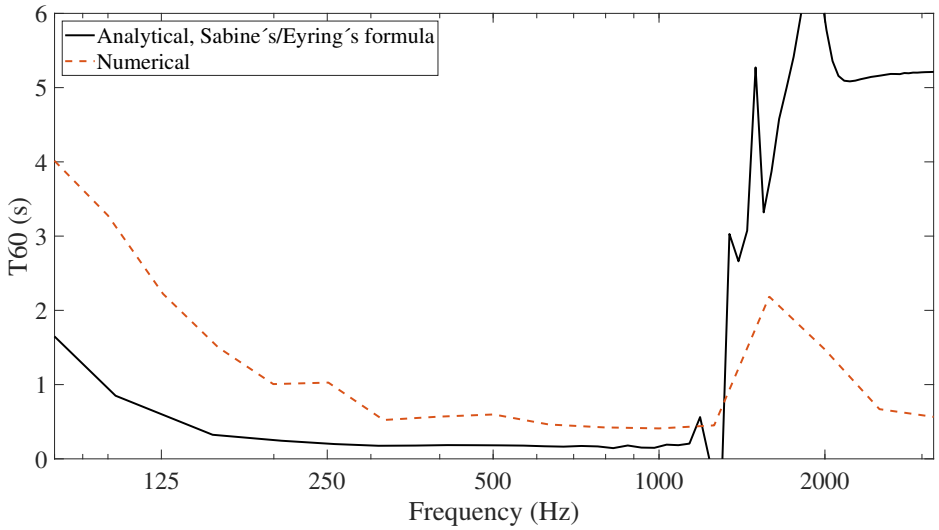

Figure 4.11: Numerically calculated reverberation time in the receiver room in third-octave bands, obtained using absorbing layers with a flow resistivity of $5 < \sigma < 500$ raylm^{-1}.

The reverberation time is generally longer in the analytically calculated case than the reverberation calculated using FDTD. Otherwise, in the range up to about 1000 Hz, both curves follow the same trend, before their intermediate difference is reduced slightly. The values of the analytical solution approximately corresponds to a common reverberation time in residential spaces, but the numerically calculated reverberation time is notably longer than that. The reason for the discrepancy might be several factors. The analytical calculations are not valid below the Schröder frequency around 125 Hz. For finding the reverberation time in the numerical case, a straight line approximation of the decay was made. For the method used, a decay of at least 30 dB is required for accuracy. The total number of samples used for this simulation were insufficient to register a decay of more than 20 dB at low frequencies. Between 250 and 1000 Hz, however, the decay was large enough. As mentioned in Section 2.3.1, steady state conditions shall be established in the room before switching off the source in order to accurately calculate the reverberation time through Schröder's backwards integration. Here, the sound source played just a short pulse.

In this study, the validating tests of the absorbing layers were performed for normal incidence. Sabine's and Eyring's formulas, however, are applied to diffuse field conditions and, by placing the spherical source inside the receiver room, there would be a natural occurrence of larger angles of incidence that are more difficult to account for. On a different note, leaks in the wall junctions have been encountered before

they were padded and are not ruled out as partial factors, even if their contribution is small.

4.5.2 Sound Pressure Level Difference

The final way to assess the performance of the room in the model is to calculate its influence on reducing the sound pressure level of an incident wave-front. In Figure 4.12, the sound pressure levels of the numerically calculated values and the result of analytical solutions in the receiving room can be seen in comparison with the sound pressure level in a receiver near the outside of the facade.

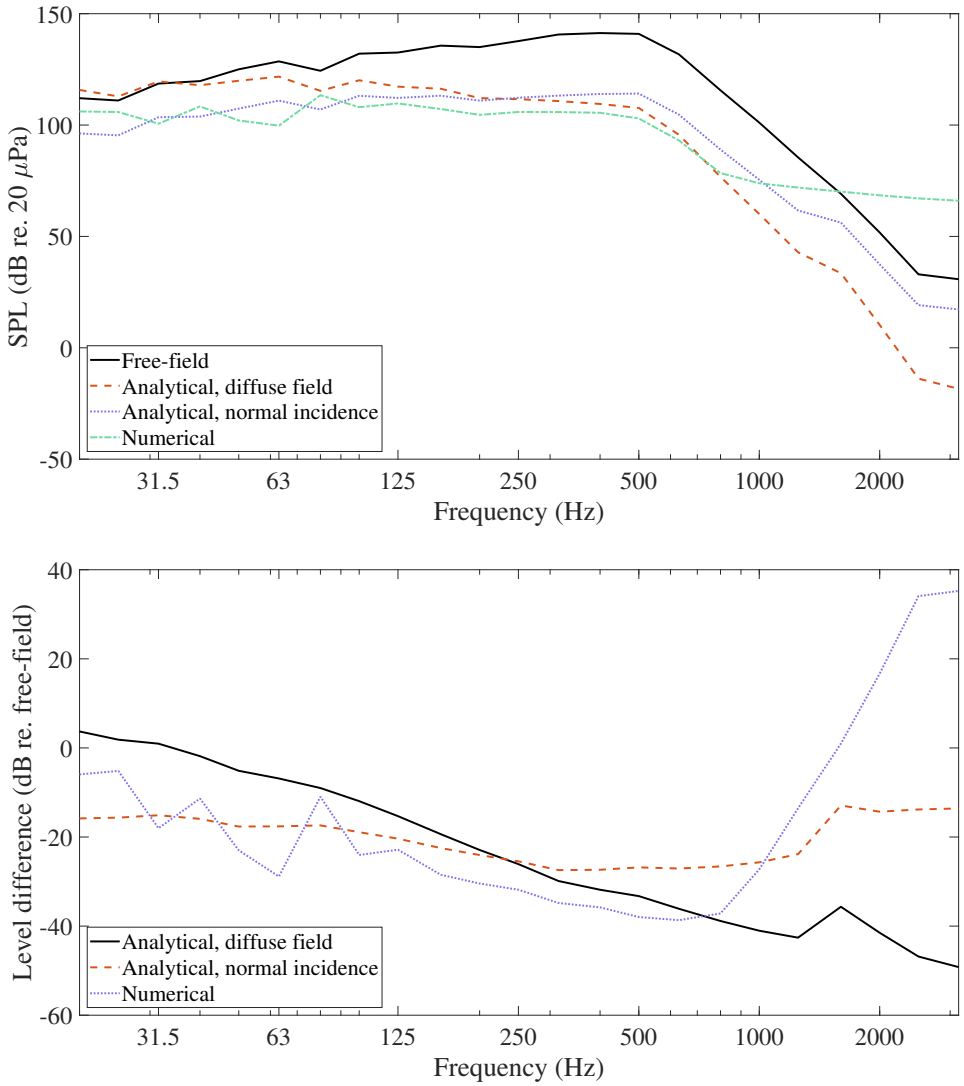

Figure 4.12: Analytically and numerically determined sound pressure levels in the receiver room along with the free-field level (top) and the difference between each indoor level and the free-field level (bottom).

The solid line in Figure 4.12 (top) represents the sound pressure levels recorded with receivers in free-field and serves as the basis for the analytical calculation of the level inside of the room. The dashed line represents the analytical solution of the sound pressure level in the receiving room, obtained through mass law calculations for sound transmission into a diffuse field. These levels are compared to numerical calculations using the FDTD model, which were obtained by averaging the level in several randomly placed receivers in the room. The numerically calculated levels are the result of transmitted sound through the facade, combined with the partially reflected sound in the receiver room.

Generally, the numerical values of the levels in the receiver room are fairly coincident with the analytical solutions. The mass law states that the sound insulation of a single-leaf construction is increased with frequency and relative to the free-field values there is a clear trend of decreased sound level at high frequencies, while the transmission through the wall is greater at low frequencies. The analytical solutions are only valid above the Schröder frequency, which is why the fluctuations due to room modes are not visible for the analytical curves. Even below the Schröder frequency, the general trend of a dropping level relative to free-field however remains for both the diffuse-field and the numerical curve. The trend is slightly more prominent for the analytic diffuse field solution; Figure 4.12 (bottom) shows that between 25 and 500 Hz, the diffuse field curve drops by 35.1 dB while the numerical solution is decreased by 32.8 dB relative to free-field. The normal incidence curve is almost flat. The reason for some of the deviations in the numerical solution could be the number of time steps, which again were insufficient for the sound to fade out completely. The previously discussed frequency based limitations of the FDTD model, which, with the chosen setup, renders values above about 1000 Hz unreliable.

The most probable reason for deviations in the valid frequency range is though the numerically calculated reverberation time, used to produce the plots above. If instead the reverberation time obatained from the absorber tests and Sabine's and Eyring's formula is utilized, the results look more promising, as shown in Figure 4.13.

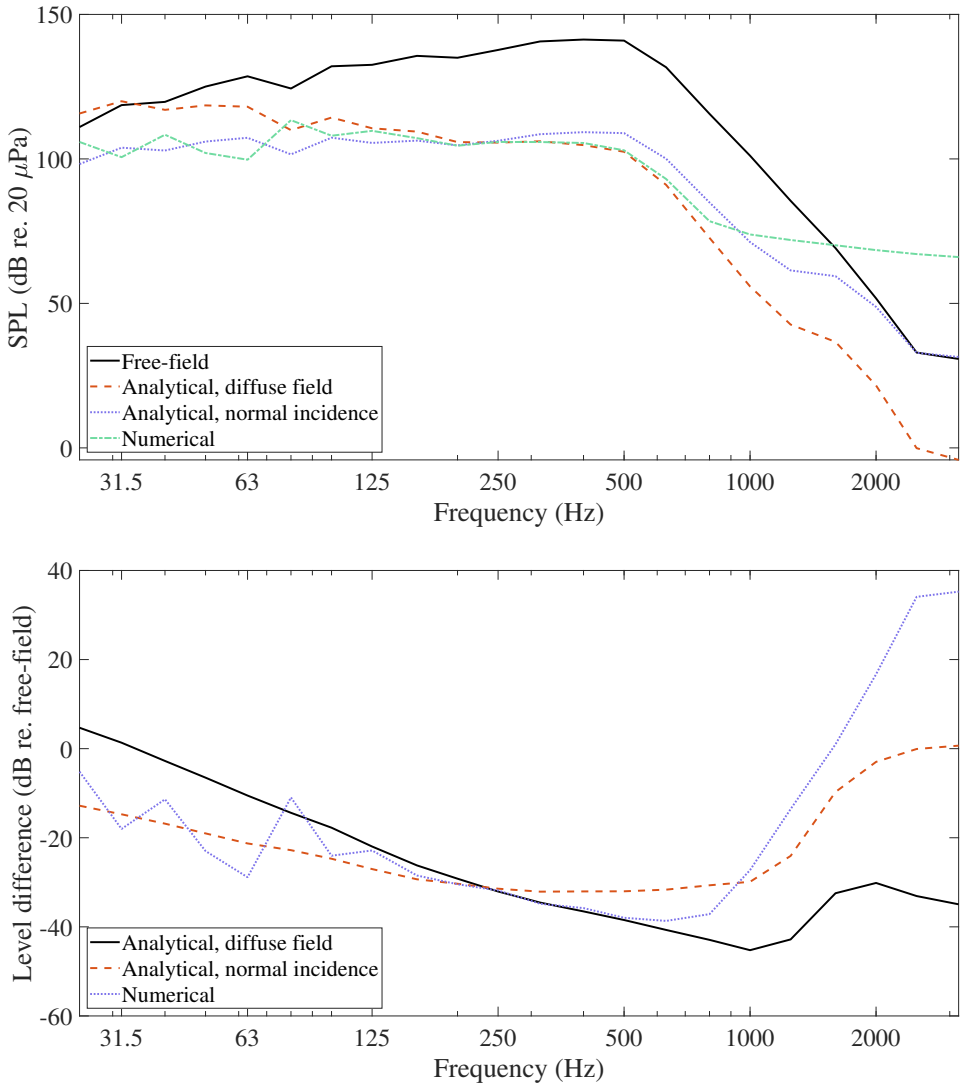

Figure 4.13: Sound pressure levels in the receiver room along with the free-field level (top) and the difference between each indoor level and the free-field level (bottom), using the reverberation time calculated through Sabine's formula for $\alpha < 0.3$ and Eyring's formula for $\alpha > 0.3$.

The analytical diffuse field solution and the numerical solution are now almost identical between 200 and 500 Hz and do not show significant deviations before around 800 Hz. This indicates that the previously mentioned estimation of the decay was unsuccessful and that additional time steps may be needed to numerically calculate the reverberation time in the room. Thus, the absorption factor and reverberation time presented in Section 4.4 could be correct, motivating further investigation of absorbing layers of this type as room absorbers in FDTD modeling.

5

Discussion

In general, three-dimensional implementation of the finite-difference time-domain method is a useful and greatly detailed way of modeling sound propagation in both outdoor and indoor spaces. From the results gathered in this study, it can be concluded that the model has good potential to simulate a large variety of features, objects and physical phenomena in a sufficiently accurate way. The sound propagation in the model is quite stable and even in every direction, without being subjected to excessive amounts of dispersion to distort the results. It is also possible to model finite-mass objects with the width of only a single node, whose space efficiency might be necessary given the apparent size requirement of other components such as the absorbing layers. The layout of the simulated area can also be easily modified and provides convenient interchangeability between the various configurations that were of interest for the study.

Although, despite the many benefits of this type of model, it is also faced with several limitations and challenges, many of which having to do with computational accuracy, efficiency and practicality. For instance, in order to get accurate results higher up in the frequency spectrum, it would seem obvious to decrease the size of the grid spacing. However, what at first sight seems like small modifications of the grid spacing can lead to largely extended computations. The more nodes that are in the grid, the more demanding and time consuming each loop iteration will be and if the number of nodes in a 3D grid is, for instance, doubled in each direction, the total number of nodes is increased by a factor 8. In addition, the temporal spacing needs to be reduced when decreasing the grid steps, leading to shorter propagation distance per time step. Thus, due to the constraints of the Courant condition, reducing the grid spacing leads to a higher demand for the amount of time steps needed in the simulation.

Another issue regarding the accuracy of the model is the modeling of porous absorbers as thick absorbing layers. As far as sound attenuation is concerned, the amount of damping that can be achieved in a layer thin enough to be placed inside of a relatively small sized room is large enough for obtaining substantial results. The main issue is rather the ability to accurately reproduce a certain absorption coefficient using a layer with increasing flow resistivity. Even if it was possible to estimate reasonable absorption coefficients, they were difficult to use for reliable and accurate reverberation time estimations as seen in Figure 4.11. The amount of time required for accurate reverberation time simulations would also prove to be longer than the capacity of the computations would allow. Naturally, that prompts further

studies and testing of the correlation between flow resistivity and the absorption coefficient in an FDTD context.

Regarding the purely visual aspects of the results, there are several improvements and upgrades that could have been applied to the current form. In terms of visualization and plotting, for instance, displaying the propagating sound as a three-dimensional sphere pulsating through a volume of air would perhaps have been a more informative and satisfying way of presenting the results of the calculations rather than as sound waves projected on a plane. Additionally, although not necessarily more descriptive, the resolution of the visual plots could have been higher. Improvements of visualization and resolution, however, come at a cost of computational capacity and calculation and simulation time which, when sufficiently marginalized, could hinder the progress and efficiency of the work.

5.1 Further Studies

Naturally, the scope of this study does not incorporate every aspect of neither FDTD simulation, nor outdoor sound propagation, that could be of interest in the case of this application. For the sake of additional studies that aim to expand the topic further, most of the components of the model could be developed and analyzed even deeper.

For example, the FDTD method could have undergone some additional testing and development as a foundation for possible alternative implementations. Although perhaps the stuff of further studies, there are other temporal discretization methods whose effect on the outcome of the calculations could have been compared in detail. To name only a few, the Aldridge method or the second order Runge-Kutta would have been interesting candidates for comparison. The performance of these methods could also be compared with each other when used in different types of media. This study focused on moving and non-moving media, but since one of the advantages of FDTD is the possibility to implement complex atmospheric parameters, a turbulent medium could for instance be the subject of another study.

The receiving end of the model, i.e. the facade and receiver room construction, also have the potential of being the subject of deeper analysis. By using multiple receiving positions, the sound pressure levels near the outside of the facade could be determined and used to calculate the wall reduction index. Such a study could even be combined with evaluations of various types of wall constructions, such as double leaf walls. It is also possible to place receivers on several height levels to simulate a multi-story apartment block and the usefulness of different noise screens for sound attenuation near such a building. Similarly, by placing receivers side by side along the length of the barrier, a finite-length noise screen could be implemented to investigate the effect of diffraction around its vertical edges. Although similar to the case of diffraction over the top of the screen, it might be of interest when considering moving sources that simulate vehicle pass-bys.

The interior of the building also proposes an area for improvement. Other than using different receiver room shapes and sizes, there could also be an interest in incorporating multi-room apartments in the model, in order to estimate how the other rooms are indirectly affected and which measures would be required to meet the various standards for acoustics in residential buildings. Another feature on the subject of room acoustics would be to develop the methods of implementing absorption in the surfaces of the room. Specifically, adapting the implementation of absorption for reverberation time calculation could prove to be particularly useful in further studies with a larger focus on the receiver room properties.

6

Conclusion

In conclusion, this study confirms several ideas about three-dimensional FDTD models of outdoor sound propagation. Firstly, it is evident from the results that a wall element with a finite mass can be implemented and behave in accordance with the mass law for sound transmission through a finite-mass screen as well as a facade element.

Furthermore, it can be concluded that absorbing boundary conditions with gradually increasing flow resistivity may serve as artificial absorbers to achieve appropriate reverberation time values for residential rooms. However, although similar tendencies were observed, the diffuse field test did not produce reverberation time results that correlated well with the analytically calculated values. Nevertheless, further studying of the absorbing layers can be motivated, since observations from other results indicated that longer simulation times would have been needed to numerically calculate the reverberation time.

The long and intensive computations are a drawback of this model, especially when considering physically large areas that are quite commonly of interest in the field of traffic noise. Its level of detail, however, could motivate its use in modeling specific situations in small, complex areas.

References

[1] Vladimir E. Ostashev. Keith Wilson. *Acoustics in Moving Inhomogeneous Media*. Taylor and Francis Group, 2 edition, 2016.

[2] Neill P. Symons. David F. Aldridge. David H. Marlin. D. Keith Wilson. Edward G. Patton. Peter P. Sullivan. Sandra L. Collier. Vladimir E. Ostashev. Douglas P. Drob. 3D staggered-grid finite-difference simulation of sound refraction and scattering in moving media. *Acoustical Society of America*, 117(2):503–517, 2005.

[3] Timothy Van Renterghem. Dick Botteldooren. Efficient FDTD-PE model for sound propagation in situations with complex obstacles and wind profiles. *ACTA Acustica united with Acustica*, 91(4):671–679, 2005.

[4] S.J. Franke. G.W. Swenson Jr. A brief tutorial on the fast field program (FFP) as applied to sound propagation in the air. *Applied Acoustics*, 27(3):203–215, 1989.

[5] D. Keith Wilson. Lanbo Liu. *Finite-Difference, Time-Domain Simulation of Sound Propagation in a Dynamic Atmosphere*. US Army Corps of Engineers, 1 edition, 2004.

[6] Vladimir E. Ostashev. D. Keith Wilson. Lanbo Liu. David F. Aldridge. Neill P. Symons. David Marlin. Equations for finite-difference time-domain simulation of sound propagation in moving inhomogeneous media and numerical implementation. *Acoustical Society of America*, 117(2):503–517, 2005.

[7] Timothy Van Renterghem. Efficient outdoor sound propagation modeling with the finite-difference time-domain (FDTD) method: a review. *Aeroacoustics*, 13(5 & 6):385–404, 2014.

[8] Jean-Pierre Berenger. A perfectly matched layer for the absorption of electromagnetic waves. *Journal of Computational Physics*, 114(2):185–200, 1994.

[9] Svensk Standard. *Acoustics – Field measurement of sound insulation in buildings and of building elements – Part 3: Façade sound insulation (ISO 16283-3:2016)*, 2016.

[10] Tor Erik Vigran. *Building Acoustics*. Taylor and Francis Group, 1 edition, 2008.

[11] M. R. Schroeder. New method of measuring reverberation time. *Acoustical Society of America*, 37(3):409–412, 1965.

[12] Keith Attenborough. Kai Ming Li. Kirill Horoshenkov. *Predicting Outdoor Sound*. Taylor and Francis Group, 1 edition, 2007.

[13] W. James Hadden Jr. Allan D. Pierce. Sound diffraction around screens and wedges for arbitrary point source locations. *The Journal of the Acoustical Society of America*, 69(5):1266–1276, 1981.

[14] D. Ouis. Noise attenuation by a hard wedge-shaped barrier. *Journal of Sound and Vibration*, 262(3):347–364, 2001.

DEPARTMENT OF APPLIED ACOUSTICS
CHALMERS UNIVERSITY OF TECHNOLOGY
Gothenburg, Sweden
www.chalmers.se

CHALMERS
UNIVERSITY OF TECHNOLOGY